

1 Fast bacterial growth reduces antibiotic accumulation and efficacy

2 Urszula Łapińska,^{1,2,*} Margaritis Voliotis,^{1,3} Ka Kiu Lee,^{1,2} Adrian Campey,^{1,2} M. Rhia L. Stone,^{4,5} Wanida
3 Phetsang,⁴ Bing Zhang,⁴ Krasimira Tsaneva-Atanasova,^{1,3,6,7} Mark A. T. Blaskovich⁴ and Stefano
4 Pagliara^{1,2,*}

5 ¹Living Systems Institute, University of Exeter, Stocker Road, Exeter EX4 4QD, UK.

6 ²Biosciences, University of Exeter, Stocker Road, Exeter EX4 4Q, UK.

7 ³Department of Mathematics, University of Exeter, Stocker Road, Exeter, UK.

8 ⁴Centre for Superbug Solutions, Institute for Molecular Bioscience, The University
9 of Queensland, 306 Carmody Road, St Lucia 4072, Brisbane, Australia.

10 ⁵Department of Chemistry and Chemical Biology, Rutgers, the State University of New Jersey, 123 Bevier
11 Rd, Piscataway, 08854, New Jersey, United States of America

12 ⁶EPSRC Hub for Quantitative Modelling in Healthcare, University of Exeter, Exeter, EX4 4QJ, UK.

13 ⁷Dept. of Bioinformatics and Mathematical Modelling, Institute of Biophysics and Biomedical Engineering,
14 Bulgarian Academy of Sciences, 105 Acad. G. Bonchev Str., 1113 Sofia, Bulgaria

15 * Stefano Pagliara & Urszula Łapińska

16 Email: s.pagliara@exeter.ac.uk; u.lapinska@exeter.ac.uk

30

Abstract

31

Phenotypic variations between individual microbial cells play a key role in the resistance of microbial pathogens to pharmacotherapies. Nevertheless, little is known about cell individuality in antibiotic accumulation. Here we hypothesize that phenotypic diversification can be driven by fundamental cell-to-cell differences in drug transport rates. To test this hypothesis, we employed microfluidics-based single-cell microscopy, libraries of fluorescent antibiotic probes and mathematical modelling. This approach allowed us to rapidly identify phenotypic variants that avoid antibiotic accumulation within populations of *Escherichia coli*, *Pseudomonas aeruginosa*, *Burkholderia cenocepacia* and *Staphylococcus aureus*. Crucially, we found that fast growing phenotypic variants avoid macrolide accumulation and survive treatment without genetic mutations. These findings are in contrast with the current consensus that cellular dormancy and slow metabolism underlie bacterial survival to antibiotics. Our results also show that fast growing variants display significantly higher expression of ribosomal promoters before drug treatment compared to slow growing variants. Drug-free active ribosomes facilitate essential cellular processes in these fast growing variants, including efflux that can reduce macrolide accumulation. Using this new knowledge, we phenotypically engineered bacterial populations by eradicating variants that displayed low antibiotic accumulation through the chemical manipulation of their outer membrane inspiring new avenues to overcome current antibiotic treatment failures.

47

Introduction

48

Phenotypic heterogeneity between genetically identical cells has been observed across all three domains of life(1,2). This heterogeneity is characterized by individual cells that display differing phenotypic traits(3,4) and permit genotypes to persist in fluctuating environments(2). Phenotypic heterogeneity in the bacterial response to antibiotics contributes to antimicrobial resistance(5–11) and the failure to effectively treat bacterial infections(12–14). Therefore, it is imperative to develop new diagnostics capable of rapidly identifying phenotypic variants that survive antibiotic treatment(15) and develop new antibiotic therapies against such phenotypic variants(16).

55

Here we hypothesize that this phenotypic diversification is driven by fundamental cell-to-cell differences in membrane transport mechanisms and their underpinning regulatory networks. In order for an antibiotic to be effective, it needs to reach its cellular target at a concentration that is inhibitory for microorganism growth(17). In gram-negative bacteria, intracellular antibiotic accumulation(17–19) is a complex biophysical phenomenon involving different physicochemical pathways and a combination of exquisitely regulated active and passive transport processes(17,20). These processes include diffusion through the outer membrane lipid bilayer(17) and porins(21,22); self-promoted uptake through the outer membrane(23); diffusion through the inner membrane lipid bilayer which displays orthogonal selection properties compared to the outer membrane(24,25); active transport via inner membrane transporters(24); efflux out of the cell(26–29); enzymatic modification or degradation(17); and eventually binding to the intracellular target.

66

Learning the rules that permit antibiotics to accumulate in gram-negative bacteria is vitally important in order to combat phenotypic and genotypic resistance to antibiotics(24,30,31). However, most permeability data are sequestered in proprietary databases(17). Moreover, such experimental datasets have often been generated via cell-free methods that permit the measurement of the diffusion rate of a compound through simplified membrane pathways(32), but care should be taken when projecting these data to the more complex accumulation dynamics in live cells(17). Live or fixed cell methodologies including radiometric, fluorometric or biochemical assays(33–35), mass spectrometry(36–42), Raman spectroscopy(43) and microspectroscopy(44–46) have also been employed to carry out antibiotic accumulation assays. These techniques generally rely on ensemble measurements that average the results obtained from a large population of microorganisms, or are derived from examining only a handful of individual bacteria. Therefore, little is known about the variability in individual drug accumulation across many single cells within a clonal population.

78

Here, we fill this fundamental gap in our knowledge by harnessing the power of microfluidics-microscopy(47,48) combined with fluorescent antibiotic-derived probes(49–51) as well as unlabelled antibiotics. This approach allows us to examine the interactions between the major classes of antibiotics and hundreds of live individual bacteria in real-time whilst they are being dosed with the drugs. Combined with mathematical modelling these data allow us to rapidly identify phenotypic variants that avoid antibiotic accumulation and are able to sustain growth in the presence of drugs without acquiring genetic mutations.

84 We show that bacteria close to the antibiotic source accumulate faster membrane-targeting antibiotics but
85 more slowly antibiotics with intracellular targets compared to bacteria further away from the antibiotic
86 source. In contrast with the current consensus that slow cell growth leads to reduced antibiotic efficacy, we
87 discover that fast growing phenotypic variants avoid macrolide accumulation due to a higher abundance of
88 both ribosomes (i.e. the drug target) and efflux pumps. We further demonstrate that chemically manipulating
89 the bacterial outer membrane permits us to phenotypically engineer bacterial populations by eradicating
90 variants that display low antibiotic accumulation. Adopting our novel approach in clinical settings to inform
91 the design of improved drug therapies could radically transform our one health approach to antimicrobial
92 resistance.

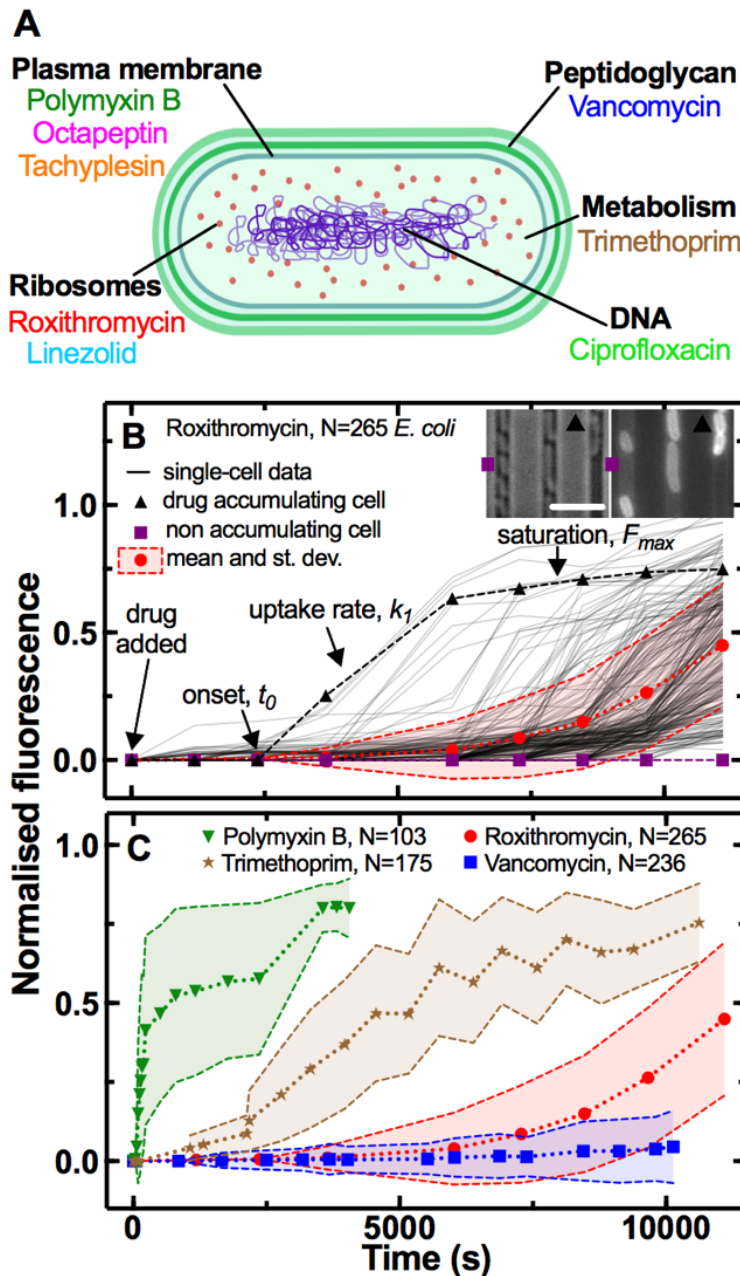
93

94 Results

95 **Experimental assessment of single-cell real-time drug accumulation dynamics**

96 We combined our recently developed single-cell microfluidics-microscopy platform(47,48,52) with
97 a library of fluorescent derivatives representing most major classes of antibiotics, including macrolides
98 (roxithromycin)(52), oxazolidinones (linezolid)(53), glycopeptides (vancomycin)(54), fluoroquinolones
99 (ciprofloxacin)(55), antifolates (trimethoprim)(56), and membrane-targeting lipopeptides/peptides
100 (polymyxin B, octapeptin, tachyplesin)(54) (Fig. 1A).

101 Each antibiotic was functionalised at a site that minimises any changes in biological activity, adding
102 a substituent that allows for facile coupling with a small fluorophore, nitrobenzoxadiazole (NBD, Table S1)
103 as previously reported(52–56). We confirmed that the majority of fluorescent derivatives retained the
104 antibiotic activity of the parent drug via minimum inhibitory concentration (MIC) assays (Table S1). Next we
105 used each probe in our microfluidics-microscopy platform(47,48,52) to quantify the dynamics of the
106 accumulation of each antibiotic in individual bacteria in real-time (Fig. 1B). Briefly, we loaded an aliquot of
107 a stationary phase clonal bacterial culture in a microfluidic device equipped with small parallel channels,
108 each hosting between one to six bacteria(47,48,52). Then we continuously flowed lysogeny broth (LB)
109 medium into the device for 2 h to stimulate cell growth and reproduction. At this point, we injected one of
110 the antibiotic probes and imaged the real-time intracellular probe accumulation in hundreds of individual
111 live bacteria (Video S1 and S2). Typically, upon onset (t_0), the uptake was initially linear (with rate constant
112 k_1), before reaching steady-state saturation levels (F_{max} , Fig. 1B) due to probe efflux, compound
113 transformation(17), or target saturation(24), although several bacteria displayed divergent accumulation
114 dynamics (Fig. 1B, S1 and S2).



115

116

117

118

119

120

121

122

123

124

125

126

127

128

129

Figure 1. Phenotypic heterogeneity in the accumulation of the major classes of antibiotics. A) Illustration depicting the eight antibiotics employed in this study alongside their bacterial targets. **B)** Accumulation of the fluorescent derivative of roxithromycin in 265 individual *E. coli* (continuous lines) after adding the probe at $46 \mu\text{g mL}^{-1}$ extracellular concentration in M9 minimal medium from $t=0$ onwards. Fluorescence values were background subtracted and normalised first by cell size and then to the maximum value in the dataset (see Methods). The circles and shaded areas represent the mean and standard deviation of the values from 265 bacteria collated from biological triplicate. The squares represent the fluorescent values of a representative bacterium that does not accumulate the fluorescent derivative of roxithromycin, whereas the triangles represent the fluorescent values of a representative bacterium that accumulates the drug. Insets: representative brightfield and fluorescence images after 7,000 s incubation in the fluorescent derivative of roxithromycin, the symbols indicate the two representative bacteria above. Scale bar: 5 μm . t_0 , k_1 and F_{max} indicate the time point at which single-cell fluorescence becomes distinguishable from the background, the rate of uptake and the final levels of accumulation at steady-state, respectively. **C)** Population average (symbols) and standard deviation (shaded areas) of the accumulation

130 of the fluorescent derivatives of polymyxin B (triangles), trimethoprim (stars), roxithromycin (circles) and
131 vancomycin (squares) probes added at 46 $\mu\text{g mL}^{-1}$ extracellular concentration in M9 minimal medium from
132 t=0 onwards. Data are obtained by averaging at least one hundred single-cell values (i.e. N=103, 175, 265
133 and 236, respectively) collated from biological triplicate. Corresponding single-cell data along with data for
134 the fluorescent derivatives of linezolid, tachyplesin, octapeptin and ciprofloxacin probes are reported in Fig.
135 S1.

136

137 **Heterogeneity in antibiotic accumulation in gram-negative and gram-positive bacteria**

138 These single-cell measurements revealed hitherto unrecognised phenotypic heterogeneity in
139 intracellular drug accumulation in clonal populations of *E. coli* as evident from the microscopy images in
140 Fig. 1B and Fig. S1. In contrast, standard techniques measure population averages of drug accumulation
141 across thousands or millions of cells(19,33,35–39,42). In our single-cell assay, population averages (circles
142 in Fig. 1B) did not reflect the fact that some phenotypic variants displayed a remarkably delayed onset,
143 slower uptake rate or reduced saturation with respect to other cells (e.g. compare the accumulation
144 trajectories reported by the squares - no accumulation - vs triangles - high accumulation - in Fig. 1B). These
145 phenotypic variants have thus far remained unrecognised in population-based experiments and give rise
146 to large coefficients of variation (CV, the ratio of the standard deviation over the mean) in the accumulation
147 of each of the eight investigated antibiotics (Fig. 1C and S3). In the following we will therefore use CV as a
148 reporter for phenotypic heterogeneity within bacterial populations as previously reported(57).

149 All bacteria within each experiment were exposed to the same concentration of probe (46 $\mu\text{g mL}^{-1}$)
150 for the same duration and to the same drug milieu, i.e. minimal medium M9 to avoid dilution of probes due
151 to cell growth(17). In accordance with previous studies about phenotypic responses to antibiotics(58,59),
152 we found that bacterial variants displaying delayed or reduced antibiotic accumulation were genuine
153 phenotypic variants, since DNA sequencing of the device outflow did not reveal any genetic mutations
154 compared to untreated bacteria. Furthermore, these variants did not display significant differences in cell
155 size (Fig. S4) and we further normalised each single-cell fluorescence value to the corresponding single-
156 cell size (see Methods)(60).

157 Due to the presence of these phenotypic variants, not all the bacteria were stained by each
158 antibiotic probe, thus we found drug-dependent dynamics in the fraction of stained bacteria (Fig. S5). The
159 lipopeptide/peptide probes targeting the outer bacterial membrane (polymyxin B, octapeptin and
160 tachyplesin) stained 90% of the investigated bacteria within 1,000 s post-addition to the microfluidic device.
161 At this time, the trimethoprim and ciprofloxacin probes targeting intracellular components had stained only
162 50% of the bacteria, whereas the number of bacteria stained by roxithromycin and vancomycin probes, with
163 a large molecular weight (1064 and 1650 g mol⁻¹, respectively), was close to zero. However, the
164 roxithromycin probe did stain 50% and 90% of the bacteria around 7,500 s and 9,000 s, respectively, post-
165 addition to the device, by which time only 15% of the bacteria had been stained by vancomycin. The lack
166 of vancomycin staining was expected since vancomycin cannot cross the gram-negative double membrane
167 to access its peptidoglycan target(61).

168 Next, we verified that this hitherto unrecognised heterogeneity in antibiotic accumulation is not a
169 phenotypic feature exclusive to *E. coli*. When we compared and contrasted roxithromycin-NBD
170 accumulation in *E. coli* against uptake in the gram-positive bacterium *S. aureus*, we found that although the
171 latter displayed more rapid accumulation dynamics (Fig. S6A and S6B, respectively), also *S. aureus*
172 displayed phenotypic variants with delayed or reduced accumulation. In fact, roxithromycin-NBD reached
173 saturation levels 3,000 s post-addition in some *S. aureus* cells, whereas other bacteria accumulated the
174 drug at very low levels and only by 5,000 s post-addition (with a CV in range 53-372% and 29-73% for *E.*
175 *coli* and *S. aureus*, respectively). In contrast, the gram-positive targeting vancomycin-NBD readily and
176 homogeneously accumulated in *S. aureus* within 2,500 s post-addition (CV in range 12-14%, Fig. S7B), but
177 did not accumulate in *E. coli* (within this same timeframe, Fig. S7A). Finally, we found phenotypic variants
178 with delayed or reduced accumulation of ciprofloxacin-NBD in three clinically-relevant gram-negative
179 bacteria: *E. coli*, *Pseudomonas aeruginosa* and *Burkholderia cenocepacia* (CV in range 12-329%, 24-534%
180 and 31-90%, Fig. S8A, S8B and S8C, respectively). Furthermore, ciprofloxacin-NBD accumulated more
181 slowly and to a lower extent in *P. aeruginosa* compared to *E. coli* and *B. cenocepacia* (Fig. S8) in
182 accordance with previous measurements at the whole population level(35) and possibly due to the high
183 porin impermeability in *P. aeruginosa*(62).

184 Finally, in order to verify that neither the drug milieu nor the concentration nor the labelling underpin
185 the observed heterogeneity in antibiotic accumulation, we run separate controls using *E. coli* and both sub-
186 inhibitory and inhibitory concentrations of roxithromycin-NBD dissolved either in M9 or LB (Fig. S9), as well
187 as unlabelled ciprofloxacin, ciprofloxacin-NBD, roxithromycin-NBD and roxithromycin-DMACA
188 (dimethylaminocoumarin-4-acetate, Fig. S10). In all cases we identified phenotypic variants with delayed
189 or reduced antibiotic accumulation, leading to large CVs as shown in Fig. S9 and Fig. S10. We can also
190 exclude possible effects of variations in magnesium availability(23,63) on the measured heterogeneity in
191 antibiotic accumulation since all bacteria were exposed to the same medium within the microfluidic device.

192

193 **Single-cell coupling between kinetic accumulation parameters**

194 Prompted by these novel findings, we moved on to an in-depth examination of antibiotic
195 accumulation dynamics and the underlying cellular and molecular mechanisms. Firstly, we developed and
196 implemented a mathematical model to rationalise these markedly heterogeneous single-cell accumulation
197 dynamics, including phenotypic variants with delayed or reduced antibiotic accumulation (see Methods).
198 Briefly, this model describes drug accumulation based on two coupled ordinary differential equations. The
199 first equation describes drug accumulation in terms of uptake, which proceeds at a time-varying rate, and
200 drug loss (due to efflux or degradation(17)), which we assume to be a first order reaction with rate constant
201 d_c . The second equation describes how the uptake rate changes over time. Here we assume a state of
202 uptake (parameter k_1 , which switches on with a time delay; parameter t_0); a linear decay term (parameter
203 d_r); as well as an adaptive inhibitory effect (parameter k_2) of the intracellular drug concentration on the
204 uptake rate (allowing us to capture the dip we observe in some single-cell trajectories in Fig. S2). We used

205 this model to fit our single-cell *E. coli* data on the accumulation of all the above investigated drugs apart
206 from vancomycin. This allowed us to compare and contrast the accumulation kinetic parameters above for
207 the different antibiotics, since we used the same probe concentration for each drug ($46 \mu\text{g mL}^{-1}$) and all
208 drugs were tested against the same clonal *E. coli* population. For vancomycin we found poor fitting for the
209 majority of cells (195 out of 241 cells), as the fluorescent signal remained indistinguishable from the
210 background, due to low cellular uptake (Fig. S1H).

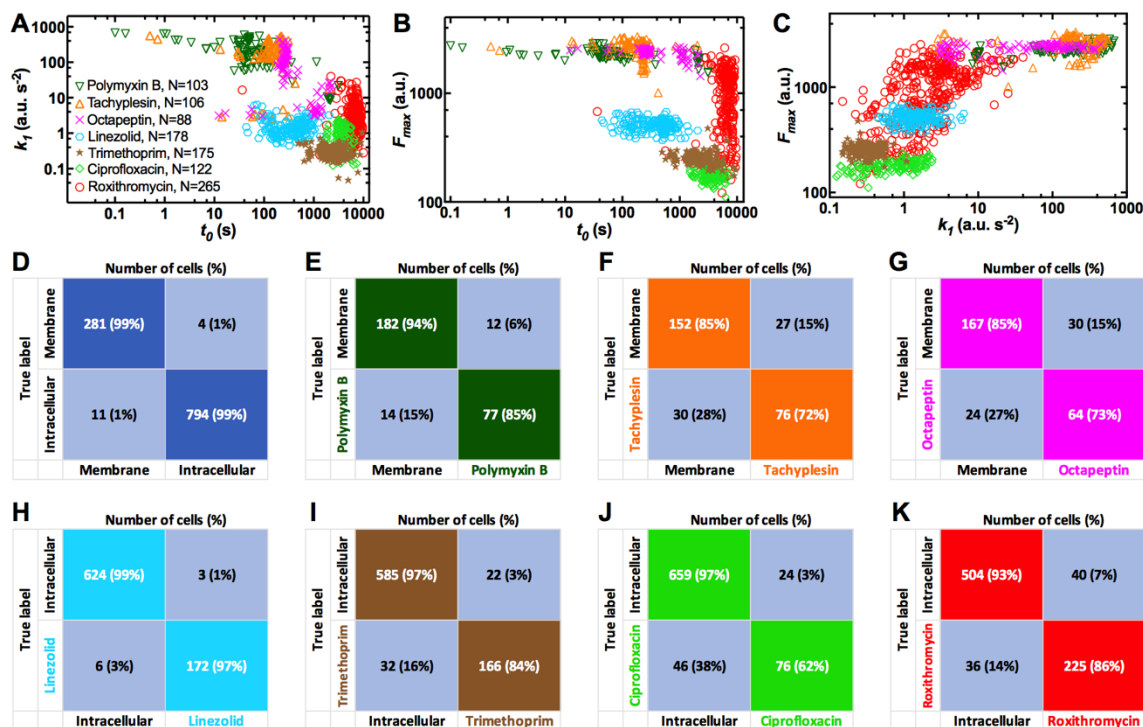
211 Membrane targeting antibiotic probes displayed on average faster accumulation onset ($t_0 = 306$,
212 364 and 571 s for tachyplesin, polymyxin B and octapeptin, respectively) compared to antibiotics with an
213 intracellular target ($t_0 = 437$, 2,525, 3,608 and 6,614 s for linezolid, trimethoprim, ciprofloxacin and
214 roxithromycin, respectively, Fig. S11). Remarkably, we found notable cell-to-cell differences in t_0 across all
215 investigated drugs with a maximum CV of 209% for polymyxin B, and a minimum CV of 25% for
216 roxithromycin (Fig. S11), further confirming the presence of phenotypic variants with delayed antibiotic
217 accumulation.

218 Membrane targeting antibiotic probes also displayed, on average, steeper rates of uptake ($k_1 =$
219 260, 229 and 93 a.u. s^{-2} for tachyplesin, polymyxin B and octapeptin, respectively) compared to antibiotics
220 with an intracellular target ($k_1 = 4.4$, 1.6, 0.9 and 0.3 a.u. s^{-2} for roxithromycin, linezolid, ciprofloxacin and
221 trimethoprim, respectively, Fig. S11). Also, k_1 was heterogeneous across all drugs investigated with a
222 maximum CV of 124% for roxithromycin and a minimum CV of 37% for trimethoprim (Fig. S11), further
223 confirming the presence of phenotypic variants with slow antibiotic uptake.

224 Membrane targeting antibiotic probes also displayed, on average, higher steady-state saturation
225 levels ($F_{max} = 2,597$, 2,357 and 2,264 a.u. for tachyplesin, octapeptin and polymyxin B, respectively)
226 compared to antibiotics with an intracellular target ($F_{max} = 1,034$, 512, 253 and 180 a.u. for roxithromycin,
227 linezolid, trimethoprim and ciprofloxacin, respectively, Fig. S11). F_{max} was also heterogeneous with a
228 maximum CV of 55% for roxithromycin and a minimum CV of 9% for octapeptin (Fig. S11) further confirming
229 the presence of phenotypic variants with reduced antibiotic accumulation. For brevity, the second order
230 kinetic parameters k_2 , d_r , and d_c are reported and discussed only in Fig. S12.

231 The finding that accumulation of membrane targeting probes happens earlier, faster and to a
232 greater extent than probes with an intracellular target can be easily rationalised considering that the latter
233 probes need to cross the gram-negative double membrane. This represents a very good validation of our
234 combined experimental and theoretical approach. However, the large heterogeneity in the kinetic
235 parameters describing the accumulation of all probes, due to phenotypic variants with delayed or reduced
236 accumulation, was instead unexpected. Additionally, the finding that roxithromycin simultaneously
237 displayed the most delayed accumulation onset but also the steepest rate of uptake and highest steady-
238 state saturation levels, across antibiotic probes with intracellular targets, was also unexpected. These data
239 corroborate the hypothesis that multiple mechanisms must be involved in intracellular antibiotic
240 accumulation at the level of the individual cell(17), a point which we expand on below.

241 Next, we used the inferred accumulation kinetic parameters to test the hypothesis that phenotypic
 242 variants within a clonal population specialise to reduce antibiotic accumulation. When we pooled together
 243 the single-cell values for all the antibiotics tested against *E. coli*, we found a strong negative correlation
 244 between t_0 and k_1 and t_0 and F_{max} , but a strong positive correlation between k_1 and F_{max} (Fig. 2A-C, Pearson
 245 coefficients $r = -0.40$, -0.27 and 0.65 , respectively, $p < 0.0001$; the relationship between k_1 and F_{max} is
 246 partially imposed by the definition of F_{max} in the model, whereas the ones between t_0 and k_1 or F_{max} are not).



247

248 **Figure 2. Single-cell coupling between key kinetic accumulation parameters.** Correlation between **A**)
 249 t_0 and k_1 , **B**) t_0 and F_{max} , **C**) k_1 and F_{max} describing the accumulation of the fluorescent derivatives of
 250 polymyxin B (downward triangles), tachyplesin (upward triangles), octapeptin (crosses), linezolid
 251 (hexagons), trimethoprim (stars), ciprofloxacin (diamonds) or roxithromycin (circles) in $N = 103, 106, 88,$
 252 $178, 175, 122, 265$ individual *E. coli*, respectively. Each data point represents the values of two kinetic
 253 parameters inferred for an individual bacterium from the data in Fig. S1 using our mathematical model.
 254 Statistical classification of the accumulation of **D**) membrane- (i.e. polymyxin B, tachyplesin and octapeptin)
 255 vs intracellular-targeting antibiotics (i.e. linezolid, trimethoprim, ciprofloxacin, roxithromycin), **E**) polymyxin
 256 B, **F**) tachyplesin or **G**) octapeptin vs the remaining membrane-targeting antibiotics, **H**) linezolid,
 257 **I**) trimethoprim, **J**) ciprofloxacin or **K**) roxithromycin vs remaining antibiotics with an intracellular target. These
 258 confusions tables are predictions generated using only the two kinetic parameters that can be rapidly
 259 measured experimentally, namely t_0 and k_1 . Similar statistical classifications were obtained when using the
 260 full set of kinetic parameters, i.e. k_2 , d_r , and d_c in addition to t_0 and k_1 .

261

262 These strong correlations show that the bacteria which start accumulating drugs later also display
 263 slow uptake and low saturation levels. This statistical analysis also reveals that i) it is possible to rapidly
 264 identify phenotypic variants displaying reduced antibiotic accumulation by inferring the whole set of kinetic
 265 parameters from a smaller subset (e.g. by inferring F_{max} from t_0 and k_1 , the latter two can be measured

266 significantly faster); ii) within a clonal bacterial population some phenotypic variants specialise to reduce
267 antibiotic accumulation in multiple ways, from delaying accumulation to reducing accumulation levels. To
268 further test this latter hypothesis, we measured the correlation between different kinetic parameters for each
269 drug data set (Fig. 2 and Table S2). We found a significantly negative correlation between t_0 and k_1 for the
270 accumulation of polymyxin B, octapeptin and roxithromycin probes; we also found a significantly negative
271 correlation between t_0 and F_{max} for the accumulation of polymyxin B, octapeptin, linezolid and trimethoprim
272 probes and a significantly positive correlation between k_1 and F_{max} for the accumulation of polymyxin B,
273 ciprofloxacin and roxithromycin probes (Fig. 2 and Table S2). Taken together these data suggest that within
274 a clonal population some phenotypic variants specialise to reduce accumulation of a wide range of
275 commonly employed antibiotics.

276 Furthermore, we also used our mathematical framework to test the hypothesis that treatment with
277 each antibiotic gives rise to a unique accumulation profile that permits identifying and classifying the
278 antibiotic in use, which is important in the context of drug development. Using statistical classification with
279 only two kinetic parameters (t_0 and k_1 , i.e. the two parameters that can be rapidly measured experimentally),
280 we found that treatment with membrane targeting probes is correctly classified against treatment with
281 intracellular targeting probes with 99% accuracy (1,075 cells analysed, Fig. 2D). Moreover, treatment with
282 polymyxin B, tachyplesin or octapeptin was correctly classified among treatments with the other two
283 membrane targeting probes with 77%, 76% and 64%, respectively (Fig. 2E-G). Finally, treatment with
284 linezolid, trimethoprim, ciprofloxacin or roxithromycin was correctly classified among treatments with the
285 other three intracellular targeting probes with 97%, 84%, 64% and 86% accuracy, respectively (Fig. 2H-K).
286 It is worth noting that we obtained similar levels of accuracy when we run such statistical classifications
287 using the full set of kinetic accumulation parameters (i.e. t_0 , k_1 , k_2 , d_r and d_c), further demonstrating that
288 measuring only t_0 and k_1 provides a good description of the antibiotic accumulation process.

289 Taken together, these data strongly suggest the existence of a unique accumulation pattern for
290 the specific antibiotic in use. Therefore our novel experimental and theoretical framework will enable the
291 classification of novel antibiotic compounds according to their kinetic accumulation parameters. As such
292 this platform could be utilized for rapid phenotyping of bacterial populations ultimately in clinical antibiotic
293 testing.

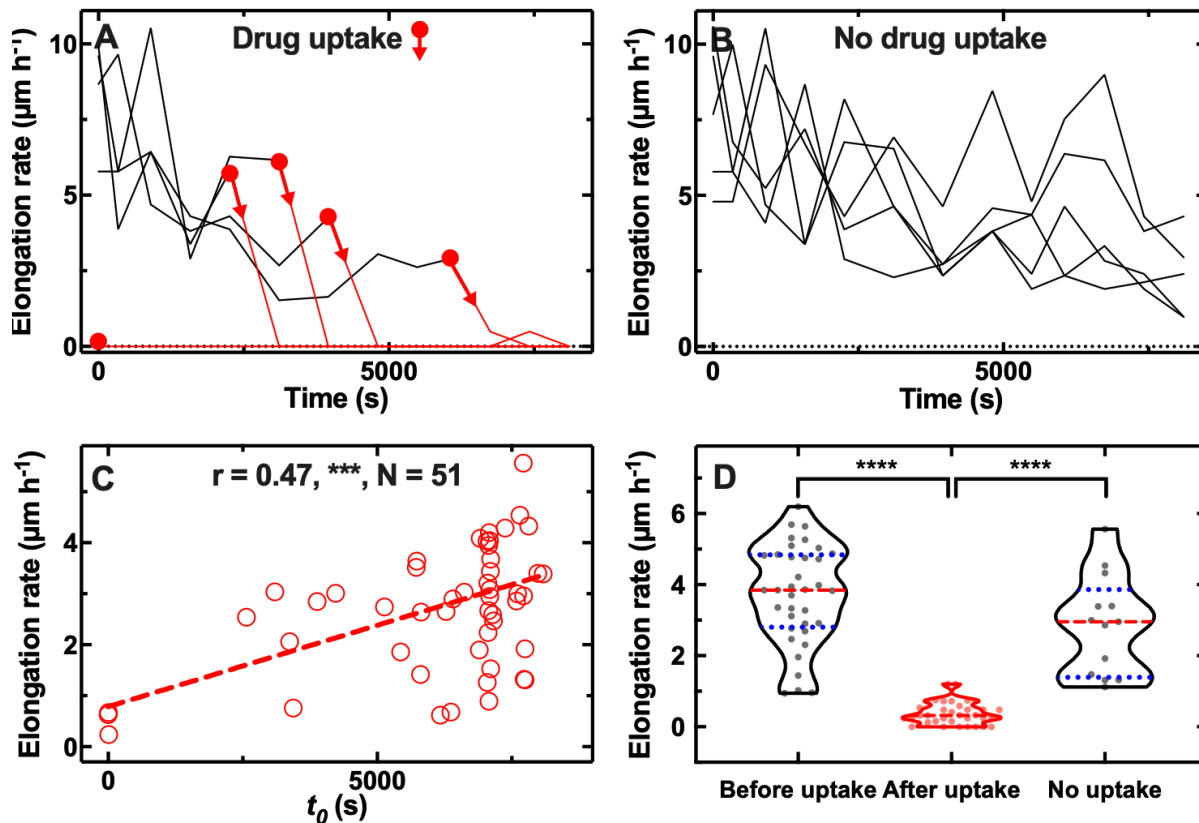
294

295 **Phenotypic variants with reduced antibiotic accumulation survive antibiotic treatment**

296 Next, we hypothesised that phenotypic variants displaying reduced antibiotic accumulation also
297 better survive antibiotic treatment, the correlation between antibiotic uptake and efficacy remaining poorly
298 investigated(17). We decided to focus on the macrolide roxithromycin since a large number of phenotypic
299 variants displayed reduced roxithromycin accumulation (Fig. S2). When we measured the elongation rate
300 of individual cells while they were being dosed with roxithromycin-NBD dissolved in LB, we found two
301 distinct cellular responses. While the majority of cells stopped growing during drug exposure (Fig. 3A),

302
303

some phenotypic variants within the same clonal *E. coli* population continued elongating for the entire duration of drug treatment (Fig. 3B).



304

305
306
307
308
309
310
311
312
313
314
315
316
317
318
319
320
321
322
323
324
325
326

Figure 3. Correlation between antibiotic efficacy and antibiotic accumulation. Temporal patterns of elongation rate during exposure to the fluorescent derivative of roxithromycin for **A**) five representative *E. coli* bacteria that accumulated the drug and **B**) five representative *E. coli* bacteria that did not accumulate the drug. The fluorescent derivative of roxithromycin was delivered at $t = 0$ at a concentration of $46 \mu\text{g mL}^{-1}$ and was dissolved in LB, circles and arrows indicate t_0 , the time point at which each bacterium started to accumulate the drug (i.e. bacterial fluorescence signal became distinguishable from the background). **C)** Correlation between each bacterium t_0 and its average elongation rate throughout exposure to the fluorescent derivative of roxithromycin (i.e. $0 < t < 8100$ s). r is the Pearson coefficient quantifying the correlation above, ***: p -value < 0.001 , $N = 52$ bacteria. **D)** Average elongation rates for bacteria that had not yet started (before uptake) or had started (after uptake) accumulating the fluorescent derivative of roxithromycin, as well as for bacteria that did not accumulate the drug (no uptake). The red dashed and blue dotted lines within each violin plot represent the median and quartiles of each data set, respectively. Paired t-test between elongation rates before and after onset in accumulation: ****, p -value < 0.0001 , $N = 36$ pairs. Unpaired t-test between the elongation rates of bacteria that did not take up the drug compared to the elongation rate of bacteria that had not yet started taking up the drug: not significant, p -value = 0.07, $N = 13$ and 36 bacteria, respectively. Unpaired t-test between the elongation rates of bacteria that did not take up the drug compared to the elongation rate of bacteria that had started taking up the drug: ****, p -value < 0.0001 , $N = 13$ and 36 bacteria, respectively.

Furthermore, there were significant cell-to-cell differences in the time at which cells stopped growing (Fig. 3A). Notably, this time coincided with the onset in roxithromycin-NBD accumulation (t_0 , indicated by circles and arrows in Fig. 3A), whereas phenotypic variants that continued growing did not

327 accumulate roxithromycin-NBD for the entire duration of the treatment (Fig. 3B). These data suggest a
328 strong link between reduced antibiotic accumulation and survival to antibiotic treatment. In fact, we found a
329 strong positive correlation between the onset of roxithromycin-NBD accumulation and the average
330 elongation rate during exposure to roxithromycin-NBD ($r = 0.49$, ***, Fig. 3C). Moreover, individual bacteria
331 that accumulated roxithromycin-NBD displayed a drastically reduced elongation rate after roxithromycin-
332 NBD accumulation started compared to their elongation rate before uptake (**** paired t-test, Fig. 3D).
333 Phenotypic variants that did not accumulate roxithromycin-NBD instead displayed an elongation rate that
334 was not significantly different compared to the elongation rate of bacteria that had not yet started taking up
335 roxithromycin-NBD (ns unpaired t-test, Fig. 3D). Finally, phenotypic variants that did not accumulate
336 roxithromycin-NBD displayed an elongation rate that was significantly higher compared to the elongation
337 rate of bacteria that had started taking up roxithromycin-NBD (**** unpaired t-test, Fig. 3D).

338 Taken together these data demonstrate that cell-to-cell differences in drug accumulation have
339 important consequences on the outcome of antibiotic therapy, prompting us to investigate the mechanisms
340 underlying phenotypic variants with delayed or reduced antibiotic accumulation.

341

342 **The microcolony architecture affects heterogeneity in antibiotic accumulation**

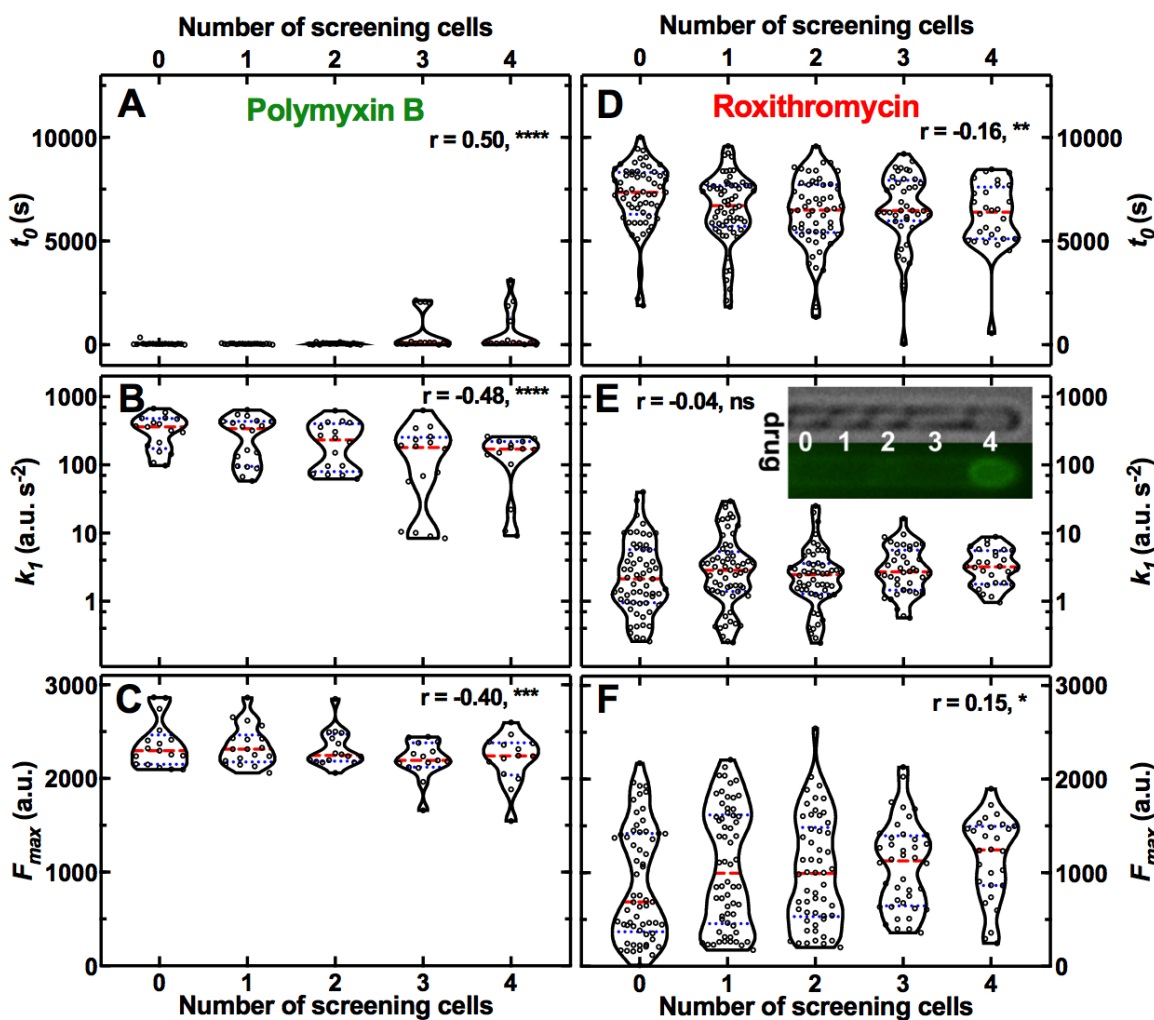
343 Firstly, we tested the hypothesis that these phenotypic variants reduced antibiotic accumulation
344 because of the presence of other bacteria (i.e. screening cells) between them and the main microfluidic
345 chamber, where the drug is injected. To test this hypothesis, we classified our data in subpopulations of
346 bacteria that had zero, one, two, three or four screening cells between themselves and the main microfluidic
347 chamber (see Inset in Fig. 4E where the drug diffuses from left to right).

348 For polymyxin B we observed that increasing the number of screening cells increased t_0 while
349 reducing k_1 and F_{max} (Pearson correlation coefficient $r = 0.50$, -0.48 and -0.40 , ****, **** and **, respectively,
350 Fig. 4A-C). Moreover, octapeptin and tachyplesin displayed strong negative correlation between k_1 and the
351 number of screening cells ($r = -0.63$ and -0.67 , respectively, ****); octapeptin also displayed a strong positive
352 correlation between t_0 and the number of screens ($r = 0.71$, ****). These data were in accordance with our
353 hypothesis that screening cells transiently decrease the pool of drug molecules available for screened cells
354 until the bacteria closer to the main chamber reach antibiotic accumulation saturation levels. These data
355 provide a mechanistic understanding for the large heterogeneity in t_0 measured for such membrane-
356 targeting probes (Fig. S11). In contrast with our hypothesis, for roxithromycin we found that increasing the
357 number of screens in front of a cell reduced t_0 and increased F_{max} ($r = -0.16$ and 0.15 , ** and *, respectively,
358 Fig. 4D-F). Moreover, both ciprofloxacin and linezolid displayed a strong negative correlation between t_0
359 and the number of screens ($r = -0.53$ and -0.28 , **** and **, respectively); ciprofloxacin also displayed a
360 strong positive correlation between k_1 and the number of screens ($r = 0.32$, **). These novel findings were
361 unexpected and were not dictated by oxygen limitation or low metabolic activity as in the case of
362 biofilms(64). In fact, we(47) and others(65) have previously demonstrated that nutrients, including oxygen

363 and metabolites, uniformly distribute across the whole length of bacteria hosting channels in our microfluidic
364 device.

365 Taken together these findings suggest non-trivial and drug-specific effects of the bacterial
366 microcolony architecture on the dynamics of drug accumulation in individual bacteria, a novel phenotypic
367 feature that should be taken into account when designing and optimising new drugs and therapies.
368 Moreover, mechanisms other than the microcolony architecture must underlie phenotypic variants with
369 reduced antibiotic accumulation. In fact, we registered significant cell-cell differences in antibiotic
370 accumulation even within the same subpopulation of bacteria with the same number of screening cells;
371 these differences were more pronounced for antibiotic with intracellular targets compared to membrane
372 targeting antibiotics (e.g. roxithromycin and polymyxin B, respectively, in Fig. 4)

373



374

375 **Figure 4. Effect of the presence of screening cells on the accumulation of antibiotics in single cells.**
376 Dependence of the kinetic parameters t_0 , k_1 , and F_{max} for the accumulation of fluorescent derivatives of
377 polymyxin B A-C) and roxithromycin D-F) on the number of screening cells between the bacterium under

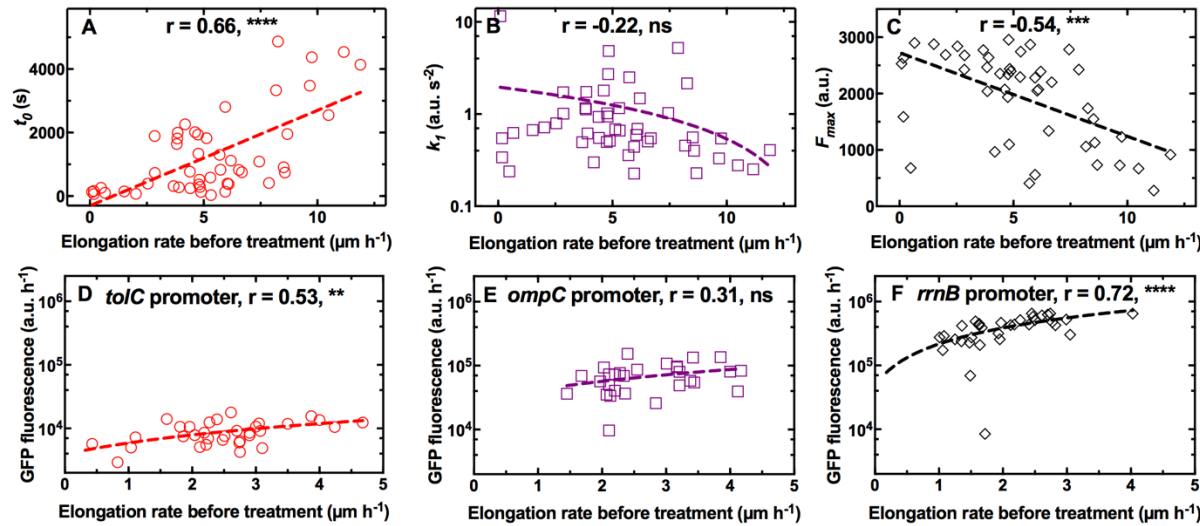
378 investigation and the main microfluidic chamber where the drug is continuously injected. Each data point is
379 the value of a kinetic parameter inferred for an individual bacterium from the data in Fig. S1 using our
380 mathematical model, $N = 103$ and 265 for polymyxin B and roxithromycin, respectively. The red dashed
381 and blue dotted lines within each violin plot represent the median and quartiles of each data set,
382 respectively. r is the Pearson coefficient quantifying the correlation between each inferred kinetic parameter
383 and the number of screening cells in front of each bacterium. ns: not significant correlation, *: p -value <
384 0.05 , **: p -value < 0.01 , ***: p -value < 0.001 , ****: p -value < 0.0001 . Inset: representative brightfield and
385 fluorescence images illustrating, from left to right, a bacterium screened by 0 , 1 , 2 , 3 , and 4 cells,
386 respectively; roxithromycin-NBD was injected in the main microfluidic chamber in the left-hand side of the
387 image and diffused from left to right. The fluorescence image shows early roxithromycin-NBD accumulation
388 in the bacterium screened by the highest number of cells.

389

390 **Cell-to-cell differences in growth rate before treatment underlie heterogeneity in antibiotic
391 accumulation**

392 In order to further dissect the mechanisms underlying phenotypic variants with reduced antibiotic
393 accumulation, we took advantage of continuous live-cell imaging to track individual bacteria for the two-
394 hour growth period in LB before incubation in each antibiotic. This permitted us to investigate links between
395 each bacterium's growth and its capability to avoid or delay antibiotic accumulation. We investigated the
396 correlation between elongation rate before treatment and the kinetic parameters describing the
397 accumulation of two representative membrane-targeting antibiotics, i.e. octapeptin and tachyplesin, and
398 two representative antibiotics with intracellular targets, i.e. trimethoprim and roxithromycin.

399 We did not find any significant correlation between single-cell elongation rate before treatment and
400 any of the kinetic parameters describing the accumulation of octapeptin and trimethoprim (Fig. S13A-C and
401 S13G-I, respectively). However, we found a positive correlation between single-cell elongation rate before
402 treatment and k_1 for tachyplesin ($r = 0.59$, **, Fig. S13E), suggesting that the latter accumulated faster in
403 fast growing cells. On the contrary, for roxithromycin, we found a significantly positive correlation between
404 single-cell elongation rate before treatment and t_0 and a significantly negative correlation between single-
405 cell elongation rate before treatment and F_{max} ($r = 0.66$ and -0.54 , **** and **, respectively, Fig. 5A and
406 5C), but no correlation with cell size (Fig. S4). Furthermore, we found that, as expected, the average
407 elongation rate significantly decreased after roxithromycin-NBD addition ($5.2 \pm 3.7 \mu\text{m h}^{-1}$ vs $3.7 \pm 2.3 \mu\text{m}$
408 h^{-1} , before and after drug addition, respectively, ****, Fig. S14A). Moreover, we also found a significantly
409 positive correlation between single-cell elongation rate before treatment and single-cell elongation rate
410 during treatment ($r = 0.34$, *, Fig. S14A). Finally, to further verify that these findings were not due to drug
411 labelling, we performed these experiments with unlabelled roxithromycin confirming a significantly positive
412 correlation between single-cell elongation rate before treatment and single-cell elongation rate during
413 treatment ($r = 0.47$, **, Fig. S14B).



414

415 **Figure 5. Differential cell growth and expression of key molecular pathways underlie heterogeneity**
416 **in roxithromycin accumulation. A-C)** Correlation between the single-cell kinetic parameters t_0 , k_1 and
417 F_{max} describing the accumulation of roxithromycin-NBD and the bacterial elongation rate during the two-
418 hour growth period preceding antibiotic treatment (see Methods). Measurements were carried out on $N =$
419 50 individual *E. coli*, collated from biological triplicate, before and after exposure to 192 $\mu\text{g mL}^{-1}$
420 roxithromycin-NBD dissolved in M9. **D-F)** Correlation between the single-cell GFP fluorescence as a proxy
421 for the expression of *tolC*, *ompC* and *rrnB* promoters and the bacterial elongation rate during the two hour
422 growth period preceding antibiotic treatment (see Methods). r is the Pearson coefficient quantifying the
423 correlation between each inferred kinetic parameter and the corresponding elongation rate of each cell. ns:
424 not significant correlation, **: p -value < 0.01 , ***: p -value < 0.001 , ****: p -value < 0.0001 . Dashed lines are
425 linear regressions to the data. Measurements were carried out on $N = 34$, 30 and 35 individual *E. coli*
426 collated from biological triplicate for the *tolC*, *ompC* and *rrnB* reporter strains, respectively.

427

428 These data demonstrate that phenotypic variants displaying reduced roxithromycin accumulation
429 are fast growing bacteria that also better survive roxithromycin treatment, thus establishing, for the first
430 time, a strong link between heterogeneity in antibiotic efficacy and cell-to-cell differences in antibiotic
431 accumulation. These novel findings are surprising considering that phenotypic survival to antibiotics has
432 traditionally been linked to slow growth, low metabolic activity and bacterial dormancy(66–68). In contrast,
433 here we show that fast growth facilitates delayed roxithromycin accumulation as well as reducing the
434 amount of macrolide accumulating in individual bacteria at steady state this decreasing roxithromycin
435 efficacy.

436

437 **Single-cell ribosome and efflux pump abundance underlies heterogeneity in macrolide**
438 **accumulation**

439 In order to determine the molecular mechanisms underpinning phenotypic variants with reduced
440 roxithromycin accumulation, we investigated whether heterogeneity in bacterial growth rate could be linked
441 to heterogeneity in the expression of key molecular pathways underlying roxithromycin accumulation. We
442 hypothesised that heterogeneity in t_0 could be linked to cell-to-cell differences in the capability to pump

443 antibiotics out from the cell, thus delaying the onset of accumulation. *tolC*, which encodes the outer
444 membrane channel of the multi-drug efflux pump AcrAB-TolC and the macrolide efflux pump MacAB-
445 TolC(17), was the most highly expressed efflux pump related gene according to our transcriptomic data of
446 *E. coli* cultures growing on LB for a period of two hours after dilution of an overnight culture (Table S3
447 and(69)). Therefore, we used a *tolC* transcriptional reporter strain(8) to establish a link between the kinetic
448 parameter t_0 , single-cell elongation rate and *tolC* expression during the two hour growth period before
449 exposure to roxithromycin. In line with our hypothesis above, we found a positive correlation between the
450 expression of *tolC* and single-cell elongation rate during the two-hour growth period before exposure to
451 roxithromycin ($r = 0.53$, **, Fig. 5D).

452 Next, we hypothesised that heterogeneity in the rate of drug uptake k_1 could be ascribed to cell-to-
453 cell differences in the expression of outer membrane porins allowing antibiotic passage across the outer
454 membrane. *ompC*, which encodes the outer membrane protein OmpC facilitating influx of several
455 antibiotics(17,70), was the most highly expressed outer membrane protein encoding gene according to our
456 transcriptomic data at the population level (Table S3 and(69)). In contrast with our hypothesis, we did not
457 find a significant correlation between *ompC* expression and single-cell elongation rate during the two-hour
458 growth period before drug exposure ($r = 0.31$, ns, Fig. 5E). These data demonstrate that bacteria growing
459 at different rates do not display significantly different levels of *ompC* expression and accordingly we did not
460 find significant correlation between cell growth and k_1 (Fig. 5B).

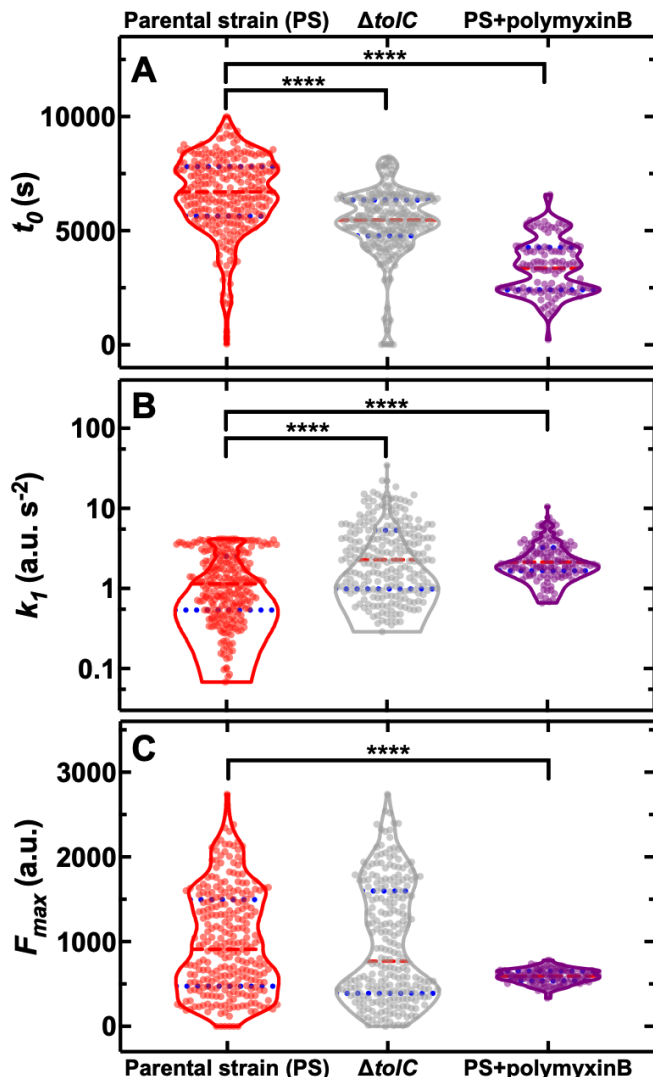
461 Finally, we hypothesised that cell growth and saturation levels in roxithromycin accumulation could
462 depend on the ribosomal content (i.e. the drug target) at the single-cell level. Accordingly, we found a strong
463 positive correlation between the expression of the ribosomal promoter *rrnB* and single-cell elongation rate
464 during the two-hour growth period before exposure to roxithromycin ($r = 0.72$, ****, Fig. 5F).

465 Taken together these data shed light on the molecular mechanisms underpinning the observed
466 heterogeneity in the intracellular accumulation of the macrolide roxithromycin: fast growing variants reduce
467 the intracellular accumulation of roxithromycin, and thus better survive treatment with this drug, via elevated
468 ribosomal content and, to a lesser extent, higher expression of efflux pumps. These data call into question
469 the current consensus that metabolically inactive or dormant bacteria better survive antibiotic challenge(66–
470 68,71).

471

472 External manipulation of the heterogeneity in antibiotic accumulation

473 Building on the molecular understanding gained above, we then set out to establish whether
474 phenotypic variants displaying reduced roxithromycin accumulation could be suppressed either genetically
475 or chemically. In order to do so, we employed a $\Delta tolC$ knock-out mutant and found that, when investigating
476 roxithromycin accumulation, t_0 was significantly lower and k_1 was significantly higher in the $\Delta tolC$ mutant
477 compared to the parental strain (Fig. 6A and 6B, respectively).



478

479
480
481
482
483
484
485
486
487
488
489
490
491
492
493

Figure 6. Genetic and chemical manipulation of heterogeneity in drug accumulation. Distributions of single-cell values for the kinetic parameters A) t_0 , B) k_1 and C) F_{max} describing the accumulation of the fluorescent derivative of roxithromycin (at 46 μ g mL^{-1} in M9) in the *E. coli* BW25113 parental strain (PS), the knock-out mutant Δ to/C and the parental strain co-treated with unlabelled polymyxin B at 1 μ g mL^{-1} extracellular concentration. The red dashed and blue dotted lines within each violin plot represent the median and quartiles of each data set, respectively. ****: p-value < 0.0001. N = 262, 241 and 116 individual parental strain *E. coli* treated with the roxithromycin probe, Δ to/C *E. coli* treated with the roxithromycin probe and parental strain *E. coli* co-treated with the roxithromycin probe and 1 μ g mL^{-1} unlabelled polymyxin B.

However, we also found Δ to/C phenotypic variants with reduced roxithromycin accumulation and even higher levels of heterogeneity in the three kinetic parameters for the Δ to/C mutant compared to the parental strain (CV of 27% vs 25%, 114% vs 80%, 72% vs 62% for t_0 , k_1 , and F_{max} , respectively, Fig. 6). These data demonstrate that targeting efflux might not be a promising avenue to reduce heterogeneity in drug accumulation and confirm that the observed heterogeneity in roxithromycin accumulation is not exclusively underpinned by cell-to-cell differences in efflux pump expression.

494 Since we demonstrated that heterogeneity in porin expression does not underpin cell-to-cell differences in
495 roxithromycin accumulation, we hypothesised that the composition and permeability of the lipid bilayer
496 making up the bacterial outer membrane could underlie heterogeneity in roxithromycin accumulation. If this
497 were true, the heterogeneity in roxithromycin accumulation could be chemically manipulated by using
498 agents that permeabilise the outer membrane, such as polymyxin B(72). Accordingly, when we treated the
499 parental strain with roxithromycin-NBD at 46 $\mu\text{g mL}^{-1}$ in combination with unlabelled polymyxin B at 1 μg
500 mL^{-1} extracellular concentration, we found a significant decrease in the heterogeneity of k_1 and F_{max}
501 compared to roxithromycin-NBD treatment alone (CV of 59% vs 80%, 14% vs 62%, respectively, Fig. 6B
502 and 6C). Additionally, the accumulation dynamics of roxithromycin-NBD in the presence of unlabelled
503 polymyxin B was significantly earlier and faster compared to that measured in the absence of polymyxin B
504 (Fig. 6). Taken together, these data suggest that phenotypic variants displaying reduced roxithromycin
505 accumulation might have a significantly more impermeable outer membrane than phenotypically
506 susceptible bacteria, possibly due to differences in lipid composition and packing and that targeting the
507 outer membrane might be a viable avenue for suppressing variants with reduced intracellular antibiotic
508 accumulation.

509

510 Discussion

511 Bacterial slow growth has often been associated with decreased antibiotic susceptibility(66,73,74)
512 with few exceptions(75,76). Moreover, a recent paper suggested that phenotypic variants accumulate lower
513 levels of phenoxycephalosporin while being in a dormant state before treatment(59). In striking contrast,
514 here we provide compelling evidence that fast growth and elevated ribosomal content better prepare
515 phenotypic variants for avoiding the intracellular accumulation of macrolides, a finding that needs to be
516 considered when designing antibiotic therapy.

517 A linear correlation between ribosomal abundance and growth rate has previously been found via
518 ensemble measurements obtained on exponentially growing *E. coli* supplied with nutrients of increasing
519 quality in the absence of antibiotics(77). Our findings enrich the current understanding of the
520 interdependence of cell growth and ribosomal content demonstrating that this correlation holds within an
521 isogenic population homogeneously exposed to the same medium.

522 Previous ensemble measurements have demonstrated that fast growth on high quality nutrients
523 decreases *E. coli* growth inhibition by antibiotics that irreversibly bind to ribosomes (such as roxithromycin
524 (78)) compared to slower growth on poor quality nutrients(79). Here, we offer a mechanistic understanding
525 of this unexpected finding, showing that reduced growth inhibition in fast growing cells is dictated by growth-
526 dependent transport rates, as fast growing variants displayed reduced macrolide accumulation. Importantly,
527 we demonstrated that this phenotypic response is found not only at the population-level(79), but also within
528 an isogenic population.

529 These new data can be rationalised by considering that in fast growing variants a fraction of leading
530 actively translating ribosomes(80) escapes roxithromycin binding, while other ribosomes stall after
531 accumulating roxithromycin. Drug-free active ribosomes continue to facilitate essential cellular processes
532 including efflux that can reduce macrolide accumulation. Accordingly, we found that before antibiotic
533 treatment fast growing variants also displayed a significantly higher expression of the efflux promoter *toC*
534 compared to slow growing cells. Moreover, the deletion knockout ΔtoC displayed significantly earlier and
535 faster accumulation of roxithromycin compared to the parental strain, confirming that roxithromycin is a
536 substrate of the AcrAB- and MacAB-TolC efflux pumps(24). However, this mutant exhibited accumulation
537 heterogeneity levels comparable to the parental strain. These data suggest that phenotypic variants reduce
538 antibiotic accumulation using processes other than efflux alone, in contrast with previous findings(59), and
539 in accordance with our data on the key role played by heterogeneity in ribosomal abundance.

540 Our data also revealed a strong correlation between the accumulation of roxithromycin and the
541 effect of this antibiotic on cell growth down to the scale of the individual cell. This suggests that phenotypic
542 variants with reduced antibiotic accumulation could be an important factor contributing to phenotypic
543 resistance to antibiotics(2,8,73,81). This fundamentally new knowledge calls for a major rethink about
544 phenotypic resistance to antibiotics that is currently centred around target deactivation or
545 modification(73,82,83) with very little known about the correlation between antibiotic accumulation and
546 antibiotic efficacy(17,59).

547 Experimental evidence suggests that both macrolides and polymyxins use the self-promoted
548 uptake pathway. Moreover, polymyxins have a higher affinity to the LPS compared to macrolides and
549 increase the permeability of the outer membrane to other freely diffusing antibiotic molecules (23).
550 Accordingly, we observed that growth-dependent transport rates were not dictated by heterogeneity in the
551 expression of OmpC, which is a major route of antibiotic influx via the hydrophilic pathway(84). Our data
552 show instead that the phenotypic variants that avoid roxithromycin accumulation can be suppressed by
553 delivering roxithromycin in combination with polymyxin B. Moreover, roxithromycin accumulated at lower
554 saturation levels in the presence of polymyxin B as expected due to competitive binding to the LPS.

555 These data suggest that heterogeneity in roxithromycin accumulation could also be due to cell-to-
556 cell differences in LPS composition. It is conceivable that phenotypic variants within the clonal population
557 might have a decreased ethanolamine content. This would result in an increased negative charge of the
558 LPS core and a decreased permeability to roxithromycin but not to polymyxin B(85) in accordance with our
559 data. It is also conceivable that phenotypic variants within the clonal population might display esterification
560 of the core-lipid A phosphates(63). However, this would result in decreased permeability to both
561 roxithromycin and polymyxin B in contrast with our data showing i) comparatively smaller cell-to-cell
562 differences in polymyxin B accumulation (beyond the heterogeneity generated by the microcolony
563 architecture) and ii) that adding polymyxin B suppresses the heterogeneity in roxithromycin accumulation.
564 Finally, it has been suggested that macrolides use the hydrophobic pathway (86). It is conceivable that

565 phenotypic variants within the clonal population might display a higher expression of *lpxA* and thus reduced
566 permeability to roxithromycin; however, this hypothesis remains to be tested.

567 We further demonstrate that the presence of phenotypic variants that avoid antibiotic accumulation
568 is not dictated by the microcolony architecture (as represented by bacterial cell position within a microfluidic
569 channel). However, our data offer a mechanistic understanding of previous work in clinical settings
570 suggesting that macrolides, quinolones, and oxazolidinones are more effective within infecting biofilms
571 compared to glycopeptides and polymyxins(64,87). In fact, we demonstrate that antibiotics with intracellular
572 targets accumulate more readily and to higher saturation levels in bacteria within the inner core of the
573 colony. In contrast, membrane targeting drugs accumulate more readily, faster and at higher saturation
574 levels in bacteria at the outer rim of the colony. This drug-specific effect of colony architecture on drug
575 accumulation must rely on growth- and efflux-independent mechanisms. In fact, we did not find significant
576 correlations between the position of a cell within the colony and neither the expression of *tolC*, *ompC* or
577 *rrnB* nor the bacterial elongation rate (p-value = 0.13, 0.13, 0.46 and 0.34, respectively).

578 In conclusion, this work reveals hitherto unrecognised phenotypic variants that avoid antibiotic
579 accumulation within bacterial populations. In contrast with the current consensus, we demonstrate that fast
580 growing phenotypic variants avoid macrolide accumulation and survive treatment due to elevated ribosomal
581 content. We show that it is possible to phenotypically engineer clonal bacterial populations by eradicating
582 phenotypic variants currently avoiding antibiotic accumulation. These data give strength to recent evidence
583 that administered doses of polymyxins can be lowered in combination therapies(40) and demonstrating that
584 roxithromycin could be repurposed against gram-negative bacteria. Finally, our novel single-cell approach
585 reveals that each antibiotic is characterised by a unique accumulation pattern and thus will in future allow
586 to classify new leading antibiotic compounds(88–91) using their kinetic accumulation parameters, guiding
587 medicinal chemistry(24) whilst avoiding biases previously introduced by activity-dependent screenings(31).

588

589 Materials and Methods

590 Chemicals and cell culture

591 All chemicals were purchased from Fisher Scientific or Sigma-Aldrich unless otherwise stated. Lysogeny
592 broth (LB) medium (10 g L⁻¹ tryptone, 5 g L⁻¹yeast extract, and 0.5 g L⁻¹ NaCl) and LB agar plates (LB with
593 15 g L⁻¹ agar) were used for planktonic growth and setting up overnight cultures. Glucose-free M9-minimal
594 media, used to dissolve fluorescent antibiotic derivatives was prepared using 5× M9 minimal salts (Merck),
595 diluted as appropriate, with additional 2 mM MgSO₄, 0.1 mM CaCl₂, 3 µM thiamine HCl in Milli-Q water.
596 Stock solutions of polymyxin B, octapeptin, tachyplesin, vancomycin, linezolid, roxithromycin and
597 trimethoprim were obtained by dissolving these compounds in dimethyl sulfoxide; ciprofloxacin instead was
598 dissolved in 0.1 M HCl in Milli-Q water. These stock solutions were prepared at a concentration of 640 µg
599 mL⁻¹. *Escherichia coli* BW25113 was purchased from Dharmacon (GE Healthcare). *ompC*, *tolC* and *rrnB*
600 reporter strains of an *E. coli* K12 MG1655 promoter library(92) were purchased from Dharmacon (GE

601 Healthcare). Plasmids were extracted and transformed into chemically competent *E. coli* BW25113 as
602 previously reported(93). *Staphylococcus aureus* ATCC 25923, *Pseudomonas aeruginosa* PA14
603 flgK::Tn5(Tcr) (the deletion of the flagellum FlgK facilitated holding cells in the hosting channel thanks to
604 the reduced bacterial motility) and *Burkholderia cenocepacia* K56-2 were kindly provided by A. Brown and
605 S. van Houte. All strains were stored in 50% glycerol stock at -80 °C. Streak plates for each strain were
606 produced by thawing a small aliquot of the corresponding glycerol stock every 2 weeks and plated onto LB
607 agar. Overnight cultures were prepared by picking a single bacterial colony from a streak plate and growing
608 it in 100 mL fresh LB medium on a shaking platform at 200 rpm and 37 °C for 17 h.

609

610 Synthesis of fluorescent derivatives of antibiotics

611 Fluorescent antibiotic derivatives from trimethoprim(56) (antifolate), linezolid(53) (oxazolidinone),
612 ciprofloxacin(55) (fluoroquinolone) and roxithromycin(52) (macrolide) were prepared as previously
613 described. Vancomycin(94) (glycopeptide), polymyxin(95) and octapeptin(96) (both lipopeptides) and
614 tachyplesin(97) (antimicrobial peptide) analogues were designed and synthesised based on structure-
615 activity-relationship studies and synthetic protocols reported in prior publications, introducing an azidolysine
616 residue for the subsequent 'click' reactions with nitrobenzoxadiazole (NBD)-alkyne. Additionally, a
617 fluorescent derivative of roxithromycin using the fluorophore dimethylamino-coumarin-4-acetate (DMACA)
618 was synthesised and used only to determine the impact of labelling on single-cell antibiotic accumulation.

619

620

621 Determination of minimum inhibitory concentration

622 Single colonies of *E. coli* BW25113 were picked and cultured overnight in cation-adjusted Mueller Hinton
623 broth (CAMHB) at 37 °C, then diluted 40-fold and grown to OD₆₀₀ = 0.5. 60 µL of each antibiotic or
624 fluorescent antibiotic derivative stocks were added to the first column of a 96-well plate. 40 µL CAMHB was
625 added to the first column, and 30 µL to all other wells. 70 µL solution was then withdrawn from the first
626 column and serially transferred to the next column until 70 µL solution withdrawn from the last column was
627 discharged. The mid-log phase cultures (i.e. OD₆₀₀ = 0.5) were diluted to 10⁶ colony forming units (c.f.u.)
628 ml⁻¹ and 30 µL was added to each well, to give a final concentration of 5×10⁵ c.f.u. ml⁻¹. Each plate contained
629 two rows of 12 positive control experiments (i.e. bacteria growing in CAMHB without antibiotics) and two
630 rows of 12 negative control experiments (i.e. CAMHB only). Plates were covered with aluminium foil and
631 incubated at 37 °C overnight. The minimum inhibitory concentrations (MICs) of fluorescent derivatives of
632 polymyxin B, octapeptin, tachyplesin, vancomycin, linezolid, roxithromycin, ciprofloxacin, trimethoprim and
633 each corresponding parental antibiotic against *E. coli* BW25113 were determined visually, with the MIC
634 being the lowest concentration well with no visible growth (compared to the positive control experiments).

635

636

Fabrication of the microfluidic devices

637

The mould for the mother machine microfluidic device(65) was obtained by pouring epoxy onto a polydimethylsiloxane (PDMS, Dow Corning) replica of the original mould containing 12 independent microfluidic chips (kindly provided by S. Jun). Each of these chips is equipped with approximately 6000 lateral microfluidic channels with width and height of 1 μm each and a length of 25 μm . These lateral channels are connected to a main microfluidic chamber that is 25 μm and 100 μm in height and width, respectively. PDMS replicas of this device were realised as previously described(98). Briefly, a 10:1 (base:curing agent) PDMS mixture was cast on the mould and cured at 70 °C for 120 min in an oven. The cured PDMS was peeled from the epoxy mould and fluidic accesses were created by using a 0.75 mm biopsy punch (Harris Uni-Core, WPI). The PDMS chip was irreversibly sealed on a glass coverslip by exposing both surfaces to oxygen plasma treatment (10 s exposure to 30 W plasma power, Plasma etcher, Diener, Royal Oak, MI, USA). This treatment temporarily rendered the PDMS and glass hydrophilic, so immediately after bonding the chip was filled with 2 μL of a 50 mg/mL bovine serum albumin solution and incubated at 37 °C for 30 min, thus passivating the internal surfaces of the device and preventing subsequent cell adhesion. We have also made available a step-by-step experimental protocol for the fabrication and handling of microfluidic devices for investigating the interactions between antibiotics and individual bacteria(99).

653

654

Imaging single-cell drug accumulation dynamics

655

An overnight culture was prepared as described above and typically displayed an optical density at 595 nm (OD₅₉₅) around 5. A 50 mL aliquot of the overnight culture above was centrifuged for 5 min at 4000 rpm and 37 °C. The supernatant was filtered twice (Medical Millex-GS Filter, 0.22 μm , Millipore Corp.) to remove bacterial debris from the solution and used to resuspend the bacteria in their spent LB to an OD₆₀₀ of 75. A 2 μL aliquot of this suspension was injected in the microfluidic device above described and incubated at 37 °C. The high bacterial concentration favours bacteria entering the narrow lateral channels from the main microchamber of the mother machine(8). We found that an incubation time between 5 and 20 min allowed filling of the lateral channels with, typically, between one and three bacteria per channel. Shorter incubation times were required for motile or small bacteria, such as *P. aeruginosa* and *S. aureus*, respectively. An average of 80% of lateral channels of the mother machine device were filled with bacteria. The microfluidic device was completed by the integration of fluorinated ethylene propylene tubing (1/32" \times 0.008"). The inlet tubing was connected to the inlet reservoir which was connected to a computerised pressure-based flow control system (MFCS-4C, Fluigent). This instrumentation was controlled by MAESFLO software (Fluigent). At the end of the 20 min incubation period, the chip was mounted on an inverted microscope (IX73 Olympus, Tokyo, Japan) and the bacteria remaining in the main microchamber of the mother machine were washed into the outlet tubing and into the waste reservoir by flowing LB at 300 $\mu\text{L h}^{-1}$ for 8 min and then at 100 $\mu\text{L h}^{-1}$ for 2 h. Bright-field images were acquired every 20 min during this 2 h period of growth in LB. Images were collected via a 60 \times , 1.2 N.A. objective (UPLSAPO60XW, Olympus) and a sCMOS camera (Zyla 4.2,

673 Andor, Belfast, UK). The region of interest of the camera was adjusted to visualise 23 lateral channels per
674 image and images of 10 different areas of the microfluidic device were acquired at each time point in order
675 to collect data from at least 100 individual bacteria per experiment. The device was moved by two
676 automated stages (M-545.USC and P-545.3C7, Physik Instrumente, Karlsruhe, Germany, for coarse and
677 fine movements, respectively). After this initial 2 h growth period in LB, the microfluidic environment was
678 changed by flowing minimal medium M9 (unless otherwise stated) with each of the NBD (unless otherwise
679 stated) fluorescent antibiotic derivatives at a concentration of 46 $\mu\text{g mL}^{-1}$ (unless otherwise stated, also
680 unlabelled ciprofloxacin was delivered at 200 $\mu\text{g mL}^{-1}$) at 300 $\mu\text{L h}^{-1}$ for 8 min and then at 100 $\mu\text{L h}^{-1}$ for 4
681 h. During this 4 h period of exposure to the fluorescent antibiotic derivative in use, upon acquiring each
682 bright-field image the microscope was switched to fluorescent mode and FITC filter using a custom built
683 Labview software. A fluorescence image was acquired by exposing the bacteria to the blue excitation band
684 of a broad-spectrum LED (CoolLED pE300white, maximal power = 200 mW Andover, UK) at 20% of its
685 intensity (with a power associated with the beam light of 7.93 mW at the sample plane). In the case of
686 unlabelled ciprofloxacin the UV excitation band of such LED was used at 100% of its intensity. These
687 parameters were adjusted in order to maximise the signal to noise ratio. Bright-field and fluorescence
688 imaging during this period was carried out every 5 min. The entire assay was carried out at 37 °C in an
689 environmental chamber (Solent Scientific, Portsmouth, UK) surrounding the microscope and microfluidics
690 equipment.

691

692

693

694 Image and data analysis

695 Images were processed using ImageJ software as previously described(47,48,100), tracking each
696 individual bacterium throughout the initial 2 h period of growth and the following 4 h period treatment with
697 each fluorescent antibiotic derivative. Briefly, during the initial 2 h growth in LB, a rectangle was drawn
698 around each bacterium in each bright-field image at every time point, obtaining its width, length and relative
699 position in the hosting microfluidic channel. Each bacterium's average elongation rate was calculated as
700 the average of the ratios of the differences in bacterial length over the lapse of time between two
701 consecutive time points. During the following 4 h incubation in the presence of the fluorescent antibiotic
702 derivative, a rectangle was drawn around each bacterium in each bright-field image at every time point
703 obtaining its width, length and relative position in the hosting microfluidic channel. The same rectangle was
704 then used in the corresponding fluorescence image to measure the mean fluorescence intensity for each
705 bacterium that is the total fluorescence of the bacterium normalised by cell size (i.e. the area covered by
706 each bacterium in our 2D images), to account for variations in antibiotic accumulation due to the cell
707 cycle(60). The same rectangle was then moved to the closest microfluidic channel that did not host any
708 bacteria in order to measure the background fluorescence due to the presence of extracellular fluorescent

709 antibiotic derivative in the media. This mean background fluorescence value was subtracted from the
710 bacterium's fluorescence value. Background subtracted values smaller than 20 a.u. were set to zero since
711 this was the typical noise value in our background measurements. All data were then analysed and plotted
712 using GraphPad Prism 8. Statistical significance was tested using either paired or unpaired, two-tailed,
713 Welch's *t*-test. Pearson correlation, means, standard deviations, coefficients of variation and medians were
714 also calculated using GraphPad Prism 8.

715

716 Inferring single-cell kinetic parameters of antibiotic accumulation via mathematical modelling

717 We constructed a minimal model of antibiotic accumulation in order to infer key kinetic parameters
718 quantifying the accumulation of each antibiotic. We modelled antibiotic accumulation using the following set
719 of ordinary differential equations (ODEs):

720

$$\frac{dc(t)}{dt} = r(t) - d_c c(t)$$
$$\frac{dr(t)}{dt} = k_1 U(t - t_0) - d_r r(t) - k_2 c(t)$$

721 where $U(t - t_0)$ represents the dimensionless step function:

722

$$U(t - t_0) = \begin{cases} 0, & t < t_0 \\ 1, & \geq t_0 \end{cases}$$

723 Variable $c(t)$ represents the intracellular antibiotic concentration (in arbitrary units [a.u.] of fluorescence
724 levels), and $r(t)$ [a.u. s^{-1}] describes the antibiotic uptake rate. With the first equation we described how
725 antibiotic accumulation, $c(t)$, changes over time as a result of two processes: (i) drug-uptake, which
726 proceeds at a time-varying rate, $r(t)$; and (ii) drug loss (efflux or antibiotic transformation), which we
727 modelled as a first order reaction with rate constant $d_c [s^{-1}]$. With the second equation we described the
728 dynamics of time-varying antibiotic uptake rate, $r(t)$. The uptake rate starts increasing with a characteristic
729 time-delay (parameter t_0), parameter $k_1 [a.u. s^{-2}]$ is the associated rate constant of this increase. We also
730 assumed a linear dampening effect (with associated rate constant $d_r [s^{-1}]$) to constrain the increase in uptake
731 rate, which allowed us to recapitulate the measured saturation in antibiotic accumulation. In this model the
732 maximum saturation is given by $F_{max} = \frac{k_1}{d_r d_c}$. Finally, we introduced an adaptive inhibitory term (rate
733 constant $k_2 [a.u. s^{-2}]$) to describe the dip we observed in some single-cell trajectories in Fig. S1 and S2
734 which we assumed is due to the fact that the presence of drugs intracellularly inhibits further drug uptake.
735 We note that in this model we did not make any a priori assumptions about the mechanisms underlying
736 antibiotic accumulation but rather aimed to capture the dynamics of the measured accumulation data.

737 Model parameters were inferred from single-cell fluorescence time-traces (see Image and data analysis
738 section) using the probabilistic programming language Stan through its python interface `pystan(101)`. Stan
739 provides full Bayesian parameter inference for continuous-variable models using the No-U-Turn sampler,
740 a variant of the Hamiltonian Monte Carlo method. All No-U-Turn parameters were set to default values

741 except parameter adapt_delta which was set to 0.999 to avoid divergent runs of the algorithm. For each
742 single-cell fluorescence time-trace the algorithm produced 4 chains, each one consisting of 3000 warmup
743 iterations followed by 1000 sampling iterations, giving in total 4000 samples from the parameters' posterior
744 distribution. For each parameter, the median of the sampled posterior is used for subsequent analysis. For
745 parameter inference, model time was rescaled by the length of the time-trace T , i.e. $t' = \frac{t}{T}$ so that time runs
746 between 0 and 1, and model parameters were re-parameterised (and made dimensionless) according to
747 the rules ($d'_c = d_c/d_r, d'_r = d_r T, k'_1 = k_1/d_r, k'_2 = k_2/d_r, t'_0 = t_0/T$). The following diffuse priors were used
748 for the dimensionless parameters, where $U(a, b)$ denotes the uniform distribution in the range
749 $[a, b]$: $d'_c \sim U(0, 1)$ so that uptake rate dynamics are always faster than drug-accumulation dynamics, i.e.,
750 $d_c < d_r$; $\log_{10} d'_r \sim U(0, 3)$ constraining the timescale associated with d_r to be shorter than the timescale of
751 the experiment, i.e., $1/d_r < T$; $\log_{10} k'_1 \sim U(0, 3)$ and $\log_{10} k'_2 \sim U(-3, 0)$, so that the parameter controlling
752 adaptive inhibition is small enough and there is no oscillatory behaviour in the model i.e., $k_2 < k_1$; $t'_0 \sim U(0, 1)$,
753 since the transformed time t' runs from 0 to 1.

754

755 Statistical classification of the accumulation of antibiotics

756 For each cell, the marginal posterior distributions of all model parameters (t_0, k_1, k_2, d_r, d_c) were summarised
757 using the corresponding first (Q_1), second (Q_2) and third (Q_3) quantiles. For each classification task, a
758 statistical model (classification decision tree) was developed for predicting the drug class for each cell using
759 the summarised parameter posterior distributions as input. Depending on the classification task, either all
760 5 parameters were considered (5x3=15 predictors) or just parameters t_0 and k_1 (2x3=6 predictors).
761 Statistical classification was performed using Matlab (method *fitctree*) and the results presented were
762 obtained using 10-fold cross-validation.

763 **Acknowledgments**

764 U.L. was supported through a BBSRC responsive mode grant (BB/V008021/1), an MRC Proximity to
765 Discovery EXCITEME2 grant (MCPC17189) and an award from the Gordon and Betty Moore Foundation
766 Marine Microbiology Initiative (GBMF5514). M.V. and K.T.A. gratefully acknowledge financial support from
767 the EPSRC via grant EP/T017856/1. K.K.L was supported via a Living Systems Institute PhD studentship.
768 A.C. was supported via an EPSRC DTP PhD studentship (EP/M506527/1). M.R.L.S. was supported by an
769 Australian Postgraduate Award and an Institute for Molecular Biosciences Research Advancement Award.
770 B.Z was supported by a CSC scholarship. M.A.T.B. was supported in part by Wellcome Trust Strategic
771 Grant WT1104797/Z/14/Z and NHMRC Development grant APP1113719. This work was further supported
772 by a Royal Society Research Grant (RG180007) awarded to S.P., a QUEX Initiator grant awarded to S.P.,
773 K.T.A. and M.A.T.B., an NHMRC Ideas grant (2004367) awarded to M.A.T.B, and a GW4 Initiator award to
774 M.V., K.T.A and S.P.. S.P.'s work in this area is also supported by a Marie Skłodowska-Curie project
775 SINGEK (H2020-MSCA-ITN-2015-675752).

776

777 **Competing interests**

778 The authors declare no competing interests.

779

780 **Author Contributions**

781 S.P. designed the research. S.P. and U.L. developed the project. U.L., K.K.L. and A.C. performed the
782 experiments. M.V. and K.T.A. developed and implemented the mathematical model. M.R.L.S., W.P., B.Z.
783 and M.B. designed and synthesised the library of fluorescent antibiotic derivatives. U.L., M.V., K.K.L., A.C.,
784 M.R.L.S., W.P., B.Z. K.T.A., M.B. and S.P. analysed and discussed the data. U.L. and S.P. wrote the paper.
785 All authors read and approved the final manuscript.

786

787

788 **References**

- 789 1. Richards TA, Massana R, Pagliara S, Hall N. Single cell ecology. *Philos Trans R Soc B Biol Sci.*
790 2019;374:20190076.
- 791 2. Ackermann M. A functional perspective on phenotypic heterogeneity in microorganisms. *Nat Rev
792 Microbiol* [Internet]. 2015;13(8):497–508. Available from: <http://dx.doi.org/10.1038/nrmicro3491>
- 793 3. Golding I, Paulsson J, Zawilski SM, Cox EC. Real-time kinetics of gene activity in individual
794 bacteria. *Cell.* 2005;123(6):1025–36.
- 795 4. Lidstrom ME, Konopka MC. The role of physiological heterogeneity in microbial population
796 behavior. *Nat Chem Biol* [Internet]. 2010;6(10):705–12. Available from:
797 <http://www.nature.com/doifinder/10.1038/nchembio.436> <http://www.ncbi.nlm.nih.gov/pubmed/20852608>
- 799 5. Windels EM, Michiels JE, Bergh B Van Den, Fauvert M, Michiels J. Antibiotics : Combatting
800 Tolerance To Stop Resistance. *MBio.* 2019;10(5):e02095.
- 801 6. Levin-reisman I, Brauner A, Ronin I, Balaban NQ. Epistasis between antibiotic tolerance ,
802 persistence , and resistance mutations. *Proc Natl Acad Sci U S A.* 2019;116:14734.
- 803 7. Brauner A, Friedman O, Gefen O, Balaban NQ. Distinguishing between resistance, tolerance and
804 persistence to antibiotic treatment. *Nat Rev Microbiol* [Internet]. 2016;14(5):320–30. Available
805 from:
806 <http://www.nature.com/doifinder/10.1038/nrmicro.2016.34> <http://www.ncbi.nlm.nih.gov/pubmed/27080241>
- 808 8. Bamford RA, Smith A, Metz J, Glover G, Titball RW, Pagliara S. Investigating the physiology of
809 viable but non-culturable bacteria by microfluidics and time-lapse microscopy. *BMC Biol.*

- 810 2017;15:121.
- 811 9. Goode O, Smith A, Łapińska U, Attrill E, Carr A, Metz J, et al. Heterologous Protein Expression
812 Favors the Formation of Protein Aggregates in Persister and Viable but Nonculturable Bacteria'.
813 ACS Infect Dis. 2021;7:1848.
- 814 10. Goormaghtigh F, Van Melderen L. Single-cell imaging and characterization of *Escherichia coli*
815 persister cells to ofloxacin in exponential cultures. Sci Adv. 2019;5(6):1–15.
- 816 11. Goode O, Smith A, Zarkan A, Cama J, Invergo BM, Belgami D, et al. Persister *Escherichia coli*
817 Cells Have a Lower Intracellular pH than Susceptible Cells but Maintain Their pH in Response to.
818 MBio. 2021;12:e00909-21.
- 819 12. Mulcahy LR, Burns JL, Lory S, Lewis K. Emergence of *Pseudomonas aeruginosa* strains
820 producing high levels of persister cells in patients with cystic fibrosis. J Bacteriol.
821 2010;192(23):6191–9.
- 822 13. Helaine S, Cheverton AM, Watson KG, Faure LM, Matthews SA, Holden DW. Internalization of
823 *Salmonella* by Macrophages Induces Formation of Nonreplicating Persisters. Science (80-).
824 2014;343:204–8.
- 825 14. Stapels DAC, Hill PWS, Westermann AJ, Fisher RA, Thurston TL, Saliba AE, et al. *Salmonella*
826 persisters undermine host immune defenses during antibiotic treatment. Science (80-).
827 2018;362(6419):1156–60.
- 828 15. Baltekin Ö, Boucharin A, Tano E, Andersson DI, Elf J. Antibiotic susceptibility testing in less than
829 30 min using direct single-cell imaging. Proc Natl Acad Sci U S A. 2017;114(34):9170–5.
- 830 16. Shatalin K, Nuthanakanti A, Kaushik A, Shishov D, Peselis A, Shamovsky I, et al. Inhibitors of
831 bacterial H₂S biogenesis targeting antibiotic resistance and tolerance. Science (80-).
832 2021;1175(June):1169–75.
- 833 17. Rybenkov V V., Zgurskaya HI, Ganguly C, Leus I V., Zhang Z, Moniruzzaman M. The Whole Is
834 Bigger than the Sum of Its Parts: Drug Transport in the Context of Two Membranes with Active
835 Efflux. Chem Rev. 2021;121:5597.
- 836 18. Van Bambeke F, Barcia-Macay M, Lemaire S, Tulkens PM. Cellular pharmacodynamics and
837 pharmacokinetics of antibiotics: Current views and perspectives. Curr Opin Drug Discov Dev.
838 2006;9(2):218–30.
- 839 19. Six DA, Krucker T, Leeds JA. Advances and challenges in bacterial compound accumulation
840 assays for drug discovery. Curr Opin Chem Biol [Internet]. 2018;44:9–15. Available from:
841 <https://doi.org/10.1016/j.cbpa.2018.05.005>
- 842 20. Zgurskaya HI, Rybenkov V V., Krishnamoorthy G, Leus I V. Trans-envelope multidrug efflux
843 pumps of Gram-negative bacteria and their synergism with the outer membrane barrier. Res

- 844 Microbiol [Internet]. 2018;169(7–8):351–6. Available from:
845 <https://doi.org/10.1016/j.resmic.2018.02.002>
- 846 21. Pagès J-M, James CE, Winterhalter M. The porin and the permeating antibiotic: a selective
847 diffusion barrier in Gram-negative bacteria. *Nat Rev Microbiol.* 2008 Dec;6(12):893–903.
- 848 22. Nestorovich EM, Danelon C, Winterhalter M, Bezrukov SM. Designed to penetrate: Time-resolved
849 interaction of single antibiotic molecules with bacterial pores. *Proc Natl Acad Sci U S A.*
850 2002;99(15):9789–94.
- 851 23. Farmer S, Li Z, Hancock REW. Influence of outer membrane mutations on susceptibility of
852 *Escherichia coli* to the dibasic macroh'de azithromycin. *J Antimicrob Chemother.* 1992;29:27–33.
- 853 24. Silver LL. Bioorganic & Medicinal Chemistry A Gestalt approach to Gram-negative entry. *Bioorg
854 Med Chem [Internet].* 2016;24(24):6379–89. Available from:
855 <http://dx.doi.org/10.1016/j.bmc.2016.06.044>
- 856 25. Cama J, Henney AM, Winterhalter M. Breaching the Barrier: Quantifying Antibiotic Permeability
857 across Gram-negative Bacterial Membranes. *J Mol Biol [Internet].* 2019;431(18):3531–46.
858 Available from: <https://doi.org/10.1016/j.jmb.2019.03.031>
- 859 26. Du D, Wang Z, James NR, Voss JE, Klimont E, Ohene-Agyei T, et al. Structure of the AcrAB-TolC
860 multidrug efflux pump. *Nature [Internet].* 2014;509(7501):512–5. Available from:
861 <http://dx.doi.org/10.1038/nature13205>
- 862 27. Blair JMA, Piddock LJV. How to measure export via bacterial multidrug resistance efflux pumps.
863 *MBio.* 2016;7(4):1–6.
- 864 28. Blair JMA, Webber MA, Baylay AJ, Ogbolu DO, Piddock LJV. Molecular mechanisms of antibiotic
865 resistance. *Nat Rev Microbiol [Internet].* 2015;13(1):42–51. Available from:
866 <http://dx.doi.org/10.1038/nrmicro3380>
- 867 29. Fitzpatrick AWP, Llabrés S, Neuberger A, Blaza JN, Bai XC, Okada U, et al. Structure of the
868 MacAB-TolC ABC-type tripartite multidrug efflux pump. *Nat Microbiol.* 2017;2(May):17070.
- 869 30. Acosta-Gutiérrez S, Ferrara L, Pathania M, Masi M, Wang J, Bodrenko I, et al. Getting Drugs into
870 Gram-Negative Bacteria: Rational Rules for Permeation through General Porins. *ACS Infect Dis.*
871 2018;4(10):1487–98.
- 872 31. Tommasi R, Brown DG, Walkup GK, Manchester JI, Miller AA. ESKAPEing the labyrinth of
873 antibacterial discovery. *Nat Rev Drug Discov.* 2015;14(8):529–42.
- 874 32. Delcour AH. Electrophysiology of bacteria. *Annu Rev Microbiol.* 2013;67:179–97.
- 875 33. Kojima S, Nikaido H. Permeation rates of penicillins indicate that *Escherichia coli* porins function
876 principally as nonspecific channels. *Proc Natl Acad Sci [Internet].* 2013;110(28):E2629–34.
877 Available from: <http://www.pnas.org/cgi/doi/10.1073/pnas.1310333110>

- 878 34. Piddock LJ V, Ricci V, Asuquo AE. Quinolone accumulation by *Pseudomonas aeruginosa*,
879 *Staphylococcus aureus* and *Escherichia coli*. *J Antimicrob Chemother*. 1999;43:61–70.
- 880 35. Asuquo AE, Piddock LJ V. Accumulation and killing kinetics of fifteen quinolones for *Escherichia*
881 *coli*, *Staphylococcus aureus* and *Pseudomonas aeruginosa*. *J Antimicrob Chemother*.
882 1993;31:865–80.
- 883 36. Zhou Y, Joubran C, Miller-Vedam L, Isabella V, Nayar A, Tentarelli S, et al. Thinking outside the
884 “bug”: A unique assay to measure intracellular drug penetration in Gram-negative bacteria. *Anal*
885 *Chem*. 2015;87(7):3579–84.
- 886 37. Richter MF, Drown BS, Andrew P, Garcia A, Shirai T, Svec RL, et al. Predictive compound
887 accumulation rules yield a broad-spectrum antibiotic. *Nature* [Internet]. 2017;545(7654):299–304.
888 Available from: <http://dx.doi.org/10.1038/nature22308>
- 889 38. Davis TD, Gerry CJ, Tan DS. General platform for systematic quantitative evaluation of small-
890 molecule permeability in bacteria. *ACS Chem Biol*. 2014;9(11):2535–44.
- 891 39. Prochnow H, Fetz V, Hotop S-K, Rivera MG, Heumann A, Brönstrup M. Subcellular quantification
892 of uptake in Gram-negative bacteria. *Anal Chem* [Internet]. 2019;91:1863. Available from:
893 <http://pubs.acs.org>
- 894 40. Brochado AR, Telzerow A, Bobonis J, Banzhaf M, Mateus A, Selkirk J, et al. Species-specific
895 activity of antibacterial drug combinations. *Nature*. 2018;559(7713):259–63.
- 896 41. Iyer R, Ye Z, Ferrari A, Duncan L, Tanudra MA, Tsao H, et al. Evaluating LC-MS/MS to measure
897 accumulation of compounds within bacteria. *ACS Infect Dis*. 2018;4:1336–45.
- 898 42. Tian H, Six DA, Krucker T, Leeds JA, Winograd N. Subcellular Chemical Imaging of Antibiotics in
899 Single Bacteria Using C60-Secondary Ion Mass Spectrometry. *Anal Chem*. 2017;89(9):5050–7.
- 900 43. Heidari-Torkabadi H, Che T, Lombardo MN, Wright DL, Anderson AC, Carey PR. Measuring
901 propargyl-linked drug populations inside bacterial cells, and their interaction with a dihydrofolate
902 reductase target, by Raman microscopy. *Biochemistry*. 2015;54(17):2719–26.
- 903 44. Vergalli J, Dumont E, Pajović J, Cinquin B, Maigre L, Masi M, et al. Spectrofluorimetric
904 quantification of antibiotic drug concentration in bacterial cells for the characterization of
905 translocation across bacterial membranes. *Nat Protoc*. 2018;13(6):1348–61.
- 906 45. Vergalli J, Dumont E, Cinquin B, Maigre L, Pajovic J, Bacqué E, et al. Fluoroquinolone structure
907 and translocation flux across bacterial membrane. *Sci Rep*. 2017;7(1):9821.
- 908 46. Vergalli J, Atzori A, Pajovic J, Dumont E, Mallochi G, Masi M, et al. The challenge of intracellular
909 antibiotic accumulation, a function of fluoroquinolone influx versus bacterial efflux. *Commun Biol*.
910 2020;3(1):1–12.
- 911 47. Lapinska U, Glover G, Capilla-lasheras P, Young AJ, Pagliara S. Bacterial ageing in the absence

- 912 of external stressors. *Philos Trans R Soc B Biol Sci.* 2019;374:20180442.
- 913 48. Cama J, Voliotis M, Metz J, Smith A, Iannucci J, Keyser UF, et al. Single-cell microfluidics
914 facilitates the rapid quantification of antibiotic accumulation in Gram-negative bacteria. *Lab Chip*
915 [Internet]. 2020;20(15):2765–75. Available from: <http://dx.doi.org/10.1039/D0LC00242A>
- 916 49. Stone MRL, Butler MS, Phetsang W, Cooper MA, Blaskovich MAT. Fluorescent Antibiotics: New
917 Research Tools to Fight Antibiotic Resistance. *Trends Biotechnol* [Internet]. 2018;36(5):523–36.
918 Available from: <http://dx.doi.org/10.1016/j.tibtech.2018.01.004>
- 919 50. Blaskovich MA, Phetsang W, Stone MRL, Lapinska U, Pagliara S, Bhalla R, et al. Antibiotic-
920 derived molecular probes for bacterial imaging. In: *Proceedings of SPIE - The International*
921 *Society for Optical Engineering.* 2019.
- 922 51. Lin L, Du Y, Song J, Wang W, Yang C. Imaging Commensal Microbiota and Pathogenic Bacteria
923 in the Gut. *Acc Chem Res.* 2021;54(9):2076–87.
- 924 52. Stone MRL, Łapińska U, Pagliara S, Masi M, Blanchfield JT, Cooper MA, et al. Fluorescent
925 macrolide probes – synthesis and use in evaluation of bacterial resistance. *RSC Chem Biol.*
926 2020;1:395–404.
- 927 53. Phetsang W, Blaskovich MAT, Butler MS, Huang JX, Zuegg J, Mamidyala SK, et al. An azido-
928 oxazolidinone antibiotic for live bacterial cell imaging and generation of antibiotic variants.
929 *Bioorganic Med Chem* [Internet]. 2014;22(16):4490–8. Available from:
930 <http://dx.doi.org/10.1016/j.bmc.2014.05.054>
- 931 54. Blaskovich MA, Phetsang W, Stone MR, Lapinska U, Pagliara S, Bhalla R, et al. Antibiotic-derived
932 molecular probes for bacterial imaging. In: *Photonic Diagnosis and Treatment of Infections and*
933 *Inflammatory Diseases II* [Internet]. 2019. p. 2. Available from:
934 <https://www.spiedigitallibrary.org/conference-proceedings-of-spie/10863/2507329/Antibiotic-derived-molecular-probes-for-bacterial-imaging/10.1117/12.2507329.full>
- 936 55. Stone MRL, Masi M, Phetsang W, Pages J-M, Cooper MA, Blaskovich MAT. Fluoroquinolone-
937 derived fluorescent probes for studies of bacterial penetration and efflux. *Medchemcomm.*
938 2019;10:901.
- 939 56. Phetsang W, Pelington R, Butler MS, Kc S, Pitt ME, Kaeslin G, et al. Fluorescent Trimethoprim
940 Conjugate Probes to Assess Drug Accumulation in Wild Type and Mutant *Escherichia coli*. *ACS*
941 *Infect Dis.* 2016;2(10):688–701.
- 942 57. Silander OK, Nikolic N, Zaslaver A, Bren A, Kikoin I, Alon U, et al. A genome-wide analysis of
943 promoter-mediated phenotypic noise in *Escherichia coli*. *PLoS Genet.* 2012;8(1).
- 944 58. Windels EM, Michiels JE, Fauvert M, Wenseleers T, Bergh B Van Den, Michiels J. Bacterial
945 persistence promotes the evolution of antibiotic resistance by increasing survival and mutation

- 946 rates. *ISME J* [Internet]. 2019; Available from: <http://dx.doi.org/10.1038/s41396-019-0344-9>

947 59. Pu Y, Zhao Z, Li Y, Zou J, Ma Q, Zhao Y, et al. Enhanced Efflux Activity Facilitates Drug
948 Tolerance in Dormant Bacterial Cells. *Mol Cell*. 2016;62(2):284–94.

949 60. Taniguchi Y, Choi PJ, Li GW, Chen H, Babu M, Hearn J, et al. Quantifying *E. coli* proteome and
950 transcriptome with single-molecule sensitivity in single cells. *Science* (80-) [Internet].
951 2010;329:533–8. Available from: <http://www.sciencemag.org/cgi/doi/10.1126/science.1188308>

952 61. Murray PR. *Manual of clinical microbiology*. American Society for Microbiology; 1995.

953 62. Ude J, Tripathi V, Buyck JM, Söderholm S, Cunrath O, Fanous J, et al. Outer membrane
954 permeability: Antimicrobials and diverse nutrients bypass porins in *Pseudomonas aeruginosa*.
955 *Proc Natl Acad Sci U S A*. 2021;118(31):1–8.

956 63. Peterson AA, Fesik SW, McGroarty EJ. Decreased binding of antibiotics to lipopolysaccharide
957 from polymyxin-resistant strains of *Escherichia coli* and *Salmonella typhimurium*. *Antimicrob
958 Agents Chemother*. 1987;31(2):230–7.

959 64. Walters III MC, Roe F, Bugnicourt A, Franklin MJ, Stewart PS. Contributions of Antibiotic
960 Penetration, Oxygen Limitation. *Antimicrob Agents Chemother*. 2003;47(1):317–23.

961 65. Wang P, Robert L, Pelletier J, Dang WL, Taddei F, Wright A, et al. Robust growth of *Escherichia*
962 *coli*. *Curr Biol* [Internet]. 2010;20(12):1099–103. Available from:
963 <http://dx.doi.org/10.1016/j.cub.2010.04.045>

964 66. Balaban NQ, Merrin J, Chait R, Kowalik L, Leibler S. Bacterial Persistence as a Phenotypic
965 Switch. *Science* (80-) [Internet]. 2004;305(September):1622–5. Available from:
966 <http://www.ncbi.nlm.nih.gov/pubmed/15308767%5Cnhttp://www.sciencemag.org/content/305/5690/1622.short>

967 67. Balaban NQ, Gerdes K, Lewis K, McKinney JD. A problem of persistence: still more questions
968 than answers? *Nat Rev Microbiol* [Internet]. 2013;11(8):587–91. Available from:
969 <http://www.ncbi.nlm.nih.gov/pubmed/24020075>

970 68. Lewis K. Persister cells, dormancy and infectious disease. *Nat Rev Microbiol* [Internet].
971 2007;5(1):48–56. Available from: <http://www.ncbi.nlm.nih.gov/pubmed/17143318>

972 69. Smith A, Kaczmar A, Bamford RA, Smith C, Frustaci S, Kovacs-Simon A, et al. The culture
973 environment influences both gene regulation and phenotypic heterogeneity in *Escherichia coli*.
974 *Front Microbiol*. 2018;9:1739.

975 70. Nikaido H. Molecular basis of bacterial outer membrane permeability revisited. *Microbiol Mol Biol
976 Rev* [Internet]. 2003;67(4):593–656. Available from:
977 [http://www.ncbi.nlm.nih.gov/article/309051&tool=pmcentrez&rendertype=abstrac](http://www.ncbi.nlm.nih.gov/article/309051)

978

979

- 980 71. Otto G. An arresting antitoxin. *Nat Rev Microbiol* [Internet]. 2021;2:41579. Available from:
981 <http://dx.doi.org/10.1038/s41579-021-00512-z>
- 982 72. Vaara M. Agents That Increase the Permeability of the Outer. *Microbiol Rev*. 1992;56(3):395–411.
- 983 73. Balaban NQ, Helaine S, Camilli A, Collins JJ, Ghigo J-M, Hardt W-D, et al. Definitions and
984 guidelines for research on antibiotic persistence. *Nat Rev Microbiol* [Internet]. 2019;17:441.
985 Available from: <http://dx.doi.org/10.1038/s41579-019-0196-3>
- 986 74. Pontes MH, Groisman EA. A physiological basis for nonheritable antibiotic resistance. *MBio*.
987 2020;11(3):1–13.
- 988 75. Orman MA, Brynildsen MP. Dormancy is not necessary or sufficient for bacterial persistence.
989 *Antimicrob Agents Chemother*. 2013;57(7):3230–9.
- 990 76. Peyrusson F, Varet H, Nguyen TK, Legendre R, Sismeiro O, Coppée JY, et al. Intracellular
991 *Staphylococcus aureus* persisters upon antibiotic exposure. *Nat Commun* [Internet].
992 2020;11(1):2200. Available from: <http://dx.doi.org/10.1038/s41467-020-15966-7>
- 993 77. Scott M, Gunderson CW, Mateescu EM, Zhang Z, Hwa T. Interdependence of Cell Growth Origins
994 and Consequences. *Science* (80-). 2010;330(November):1099–102.
- 995 78. Dinos GP, Connell SR, Nierhaus KH, Kalpaxis DL. Erythromycin, roxithromycin, and
996 clarithromycin: Use of slow-binding kinetics to compare their in vitro interaction with a bacterial
997 ribosomal complex active in peptide bond formation. *Mol Pharmacol*. 2003;63(3):617–23.
- 998 79. Greulich P, Scott M, Evans MR, Allen RJ. Growth-dependent bacterial susceptibility to ribosome-
999 targeting antibiotics. *Mol Syst Biol*. 2015;11:796.
- 1000 80. Dai X, Zhu M, Warren M, Balakrishnan R, Patsalo V, Okano H, et al. Reduction of translating
1001 ribosomes enables *Escherichia coli* to maintain elongation rates during slow growth. *Nat Microbiol*.
1002 2016;2(December 2016):16231.
- 1003 81. Wilmaerts D, Windels EM, Verstraeten N, Michiels J. General Mechanisms Leading to Persister
1004 Formation and Awakening. *Trends Genet* [Internet]. 2019;1–11. Available from:
1005 <https://doi.org/10.1016/j.tig.2019.03.007>
- 1006 82. Gollan B, Grabe G, Michaux C, Helaine S. Bacterial Persisters and Infection : Past , Present , and
1007 Progressing. *Annu Rev ofMicrobiology*. 2019;73:359.
- 1008 83. Defraine V, Fauvert M, Michiels J. Fighting bacterial persistence: Current and emerging anti-
1009 persister strategies and therapeutics Valerie. *Drug Resist Updat* [Internet]. 2018;38:12. Available
1010 from: <https://doi.org/10.1016/j.drup.2018.03.002>
- 1011 84. Delcour AH. Outer Membrane Permeability and Antibiotic Resistance. *Biochim Biophys Acta*.
1012 2009;1794(5):808–16.

- 1013 85. Clark D. Novel antibiotic hypersensitive mutants of *Escherichia coli* genetic mapping and chemical
1014 characterization. *FEMS Microbiol Lett.* 1984;21(2):189–95.
- 1015 86. Vaara M. Outer membrane permeability barrier to azithromycin, clarithromycin, and roxithromycin
1016 in gram-negative enteric bacteria. *Antimicrob Agents Chemother.* 1993;37(2):354–6.
- 1017 87. Wu H, Moser C, Wang HZ, Høiby N, Song ZJ. Strategies for combating bacterial biofilm infections.
1018 *Int J Oral Sci.* 2015;7(July 2014):1–7.
- 1019 88. Kepiro IE, Marzuoli I, Hammond K, Ba X, Lewis H, Shaw M, et al. Engineering Chirally Blind
1020 Protein Pseudocapsids into Antibacterial Persisters. *ACS Nano.* 2020;14:1609.
- 1021 89. Hammond K, Cipcigan F, Al Nahas K, Losasso V, Lewis H, Cama J, et al. Switching Cytolytic
1022 Nanopores into Antimicrobial Fractal Ruptures by a Single Side Chain Mutation. *ACS Nano.* 2021;
- 1023 90. Nonejuie P, Burkart M, Pogliano K, Pogliano J. Bacterial cytological profiling rapidly identifies the
1024 cellular pathways targeted by antibacterial molecules. *Proc Natl Acad Sci U S A.*
1025 2013;110(40):16169–74.
- 1026 91. Stokes JM, Yang K, Swanson K, Jin W, Cubillos-Ruiz A, Donghia NM, et al. A Deep Learning
1027 Approach to Antibiotic Discovery. *Cell* [Internet]. 2020;180(4):688-702.e13. Available from:
1028 <https://doi.org/10.1016/j.cell.2020.01.021>
- 1029 92. Zaslaver A, Bren A, Ronen M, Itzkovitz S, Kikoin I, Shavit S, et al. A comprehensive library of
1030 fluorescent transcriptional reporters for *Escherichia coli*. *Nat Methods.* 2006;3(8):623–8.
- 1031 93. Henry TC, Brynildsen MP. Development of Persister-FACSeq: a method to massively parallelize
1032 quantification of persister physiology and its heterogeneity. *Sci Rep* [Internet]. 2016;6(April):25100.
1033 Available from: <http://www.nature.com/articles/srep25100>
- 1034 94. Blaskovich MAT, Hansford KA, Gong Y, Butler MS, Muldoon C, Huang JX, et al. Protein-inspired
1035 antibiotics active against vancomycin- and daptomycin-resistant bacteria. *Nat Commun* [Internet].
1036 2018;9(1):22. Available from: <http://dx.doi.org/10.1038/s41467-017-02123-w>
- 1037 95. Gallardo-Godoy A, Muldoon C, Becker B, Elliott AG, Lash LH, Huang JX, et al. Activity and
1038 Predicted Nephrotoxicity of Synthetic Antibiotics Based on Polymyxin B. *J Med Chem.*
1039 2016;59(3):1068–77.
- 1040 96. Velkov T, Gallardo-Godoy A, Swarbrick JD, Blaskovich MAT, Elliott AG, Han M, et al. Structure,
1041 Function, and Biosynthetic Origin of Octapeptin Antibiotics Active against Extensively Drug-
1042 Resistant Gram-Negative Bacteria. *Cell Chem Biol.* 2018;25(4):380-391.e5.
- 1043 97. Edwards IA, Elliott AG, Kavanagh AM, Blaskovich MAT, Cooper MA. Structure-Activity and
1044 α Toxicity Relationships of the Antimicrobial Peptide Tachyplesin-1. *ACS Infect Dis.*
1045 2017;3(12):917–26.
- 1046 98. Locatelli E, Pierno M, Baldovin F, Orlandini E, Tan Y, Pagliara S. Single-File Escape of Colloidal

- 1047 Particles from Microfluidic Channels. *Phys Rev Lett* [Internet]. 2016;117(3):038001. Available
1048 from: <http://link.aps.org/doi/10.1103/PhysRevLett.117.038001>
- 1049 99. Cama J, Pagliara S. Microfluidic Single-Cell Phenotyping of the Activity of Peptide-Based
1050 Antimicrobials. In: *Polypeptide Materials: Methods and Protocols Methods in Molecular Biology*.
1051 2021. p. 237–53.
- 1052 100. Smith A, Metz J, Pagliara S. MMHelper: An automated framework for the analysis of microscopy
1053 images acquired with the mother machine. *Sci Rep*. 2019;9(1).
- 1054 101. Carpenter B, Gelman A, Hoffman MD, Lee D, Goodrich B, Betancourt M, et al. Stan: A
1055 probabilistic programming language. *J Stat Softw*. 2017;76(1).
- 1056

Fast bacterial growth reduces antibiotic accumulation and efficacy

Urszula Łapińska,^{1,2,*} Margaritis Voliotis,^{1,3} Ka Kiu Lee,^{1,2} Adrian Campey,^{1,2} M. Rhia L. Stone,^{4,5} Wanida Phetsang,⁴ Bing Zhang,⁴ Krasimira Tsaneva-Atanasova,^{1,3,6,7} Mark A. T. Blaskovich⁴ and Stefano Pagliara^{1,2,*}

¹Living Systems Institute, University of Exeter, Stocker Road, Exeter EX4 4QD, UK.

²Biosciences, University of Exeter, Stocker Road, Exeter EX4 4Q, UK.

³Department of Mathematics, University of Exeter, Stocker Road, Exeter, UK.

⁴Centre for Superbug Solutions, Institute for Molecular Bioscience, The University of Queensland, 306 Carmody Road, St Lucia 4072, Brisbane, Australia.

⁵Department of Chemistry and Chemical Biology, Rutgers, the State University of New Jersey, 123 Bevier Rd, Piscataway, 08854, New Jersey, United States of America

⁶EPSRC Hub for Quantitative Modelling in Healthcare, University of Exeter, Exeter, EX4 4QJ, UK.

⁷Dept. of Bioinformatics and Mathematical Modelling, Institute of Biophysics and Biomedical Engineering, Bulgarian Academy of Sciences, 105 Acad. G. Bonchev Str., 1113 Sofia, Bulgaria

* Stefano Pagliara & Urszula Łapińska

Email: u.lapinska@exeter.ac.uk, s.pagliara@exeter.ac.uk

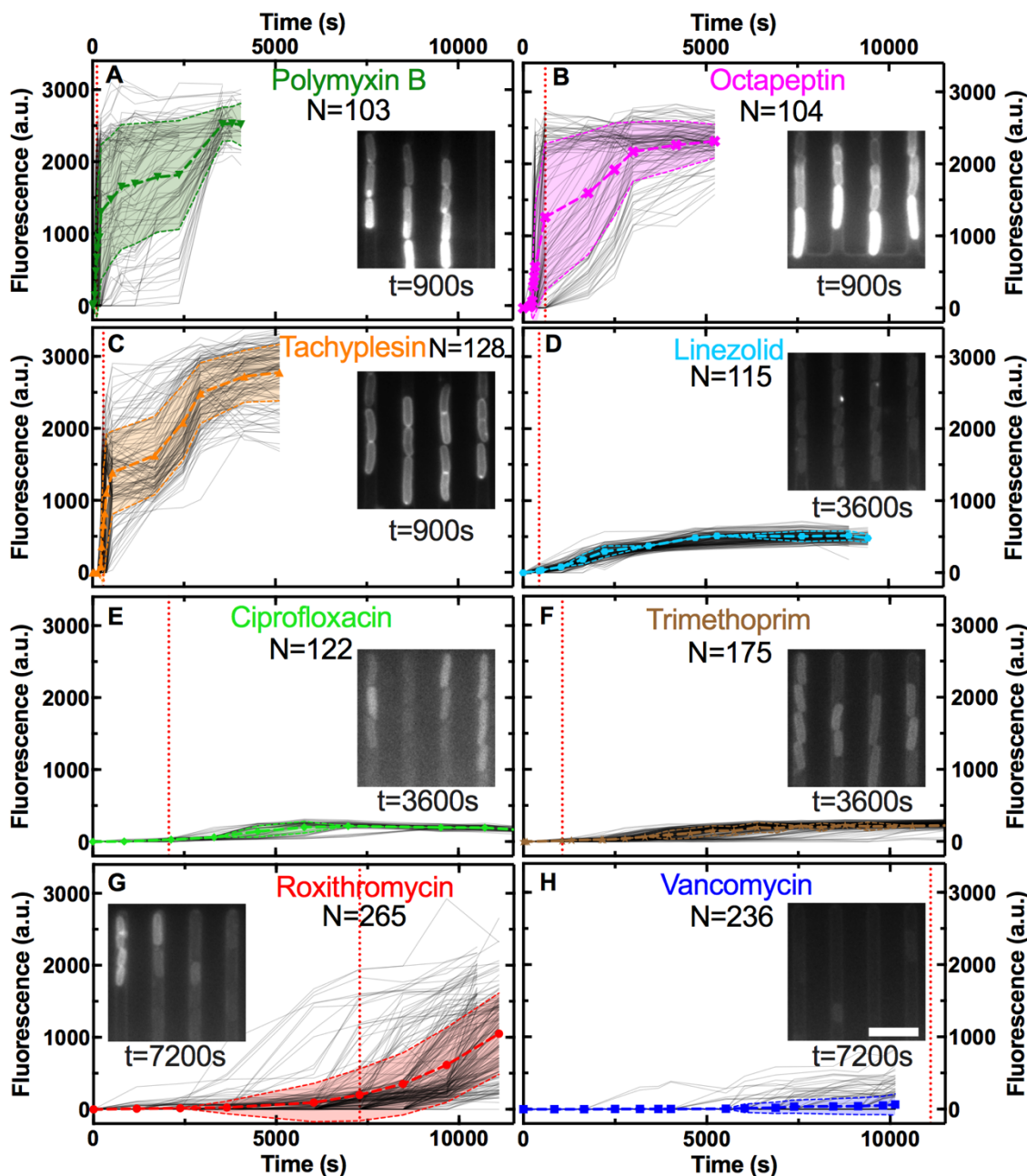


Figure S1. Accumulation of the fluorescent derivatives of **A)** polymyxin B, **B)** octapeptin, **C)** tachyplesin, **D)** linezolid, **E)** ciprofloxacin, **F)** trimethoprim, **G)** roxithromycin and **H)** vancomycin in 103, 104, 128, 115, 122, 175, 265 and 236 individual *E. coli*, respectively (continuous lines), after adding each probe at $46 \mu\text{g mL}^{-1}$ extracellular concentration in M9 minimal medium from $t = 0$ onwards. Data were collated from biological triplicate. Fluorescence values were background subtracted and normalised by cell size (see Methods). The symbols and shaded areas represent the mean and standard deviation of the corresponding single-cell values. Insets: representative fluorescence images showing the accumulation of each probe at the specific time point. Scale bar: 5 μm . The vertical dotted lines represent the time point at which the median

of each dataset became larger than zero. The median remained zero throughout the entire experiments carried out with vancomycin-NBD, hence the dotted line has been arbitrarily set at 11,500 s in **H**) for comparison purposes only.

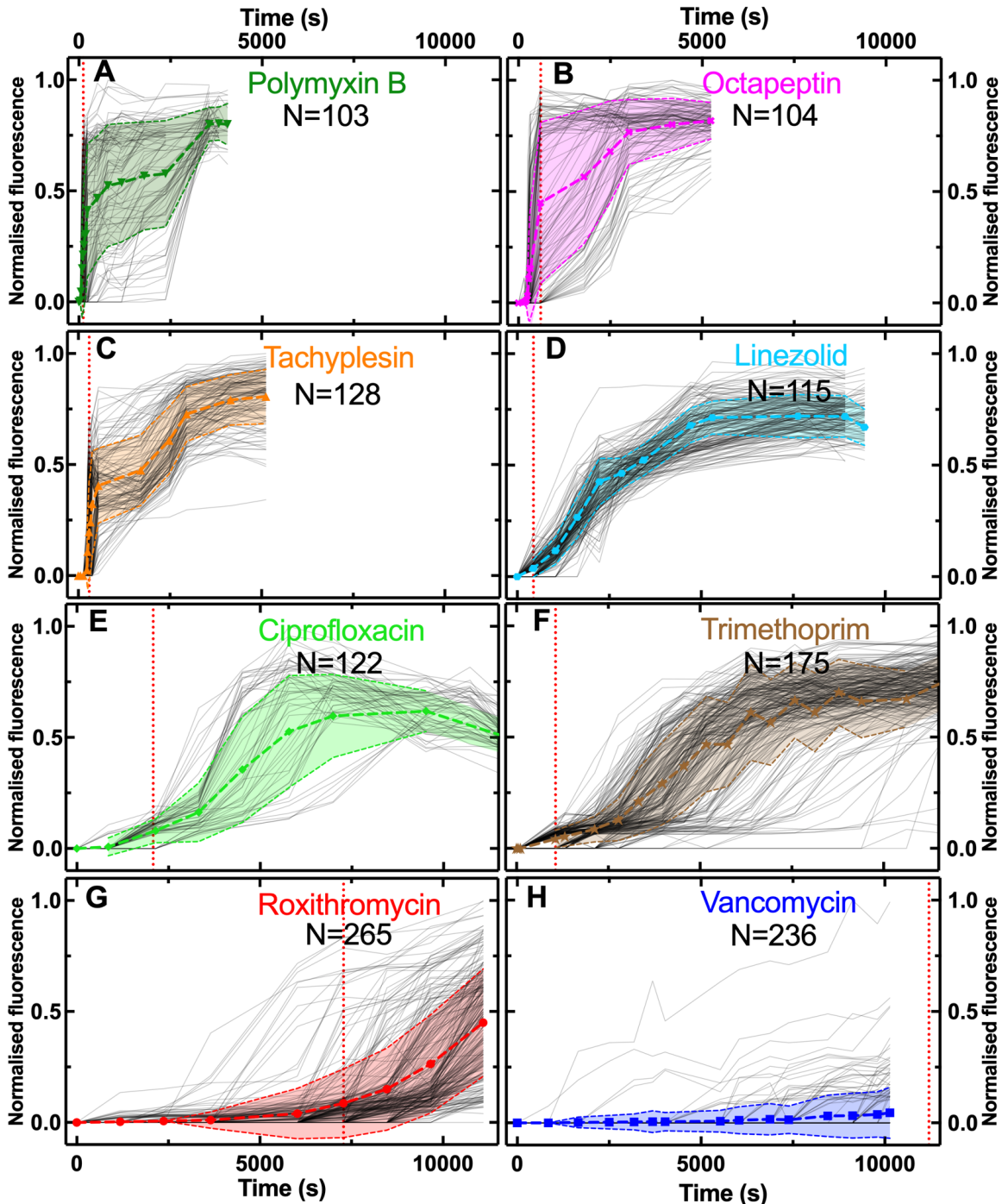


Figure S2. Normalised accumulation of the fluorescent derivatives of **A)** polymyxin B, **B)** octapeptin, **C)** tachyplesin, **D)** linezolid, **E)** ciprofloxacin, **F)** trimethoprim, **G)** roxithromycin and **H)** vancomycin. These data are reproduced from Fig. S1 after normalising all fluorescent values to the maximum fluorescence value in each dataset.

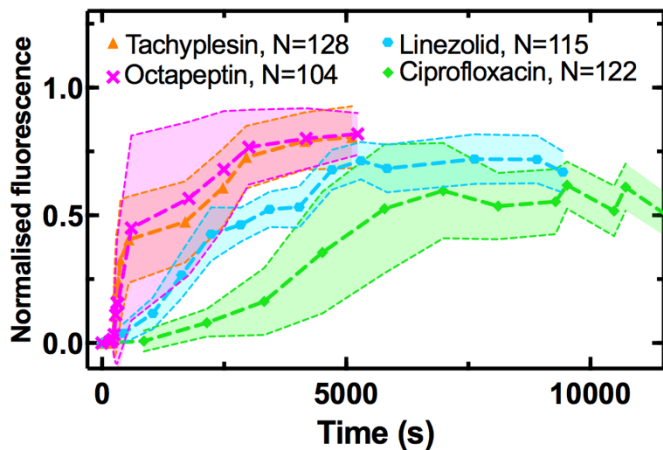


Figure S3. Population averages (symbols) and standard deviations (shaded areas) of the accumulation of the fluorescent derivatives of tachyplesin (triangles), octapeptin (crosses), linezolid (hexagons) and ciprofloxacin (diamonds) added at $46 \mu\text{g mL}^{-1}$ extracellular concentration in M9 minimal medium from $t = 0$ onwards. Data were obtained by averaging $N = 128, 104, 115$ and 122 single-cell values, respectively, collated from biological triplicate presented in Fig. S1.

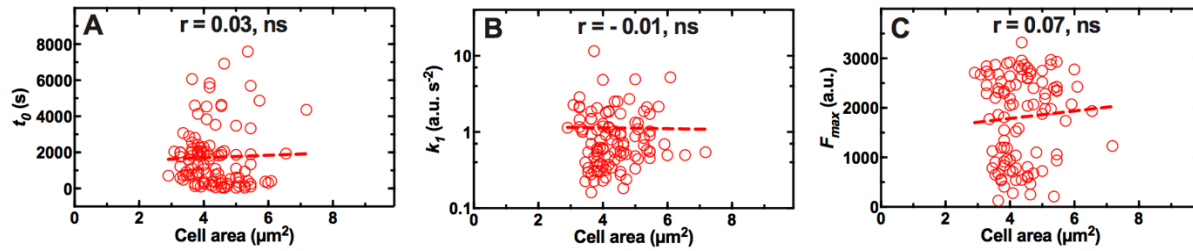


Figure S4. Absence of correlation between the area of each single bacterium before antibiotic treatment and the kinetic parameters **A)** t_0 , **B)** k_1 and **C)** F_{max} describing the onset, uptake rate and level of saturation of the fluorescent derivative of roxithromycin in $N = 104$ *E. coli* after adding the probe at $192 \mu\text{g mL}^{-1}$ extracellular concentration in M9 minimal medium from $t = 0$ onwards. Data were collated from biological triplicate. We also found no correlation between cell area and the three kinetic accumulation parameters above for the other seven antibiotic probes investigated.

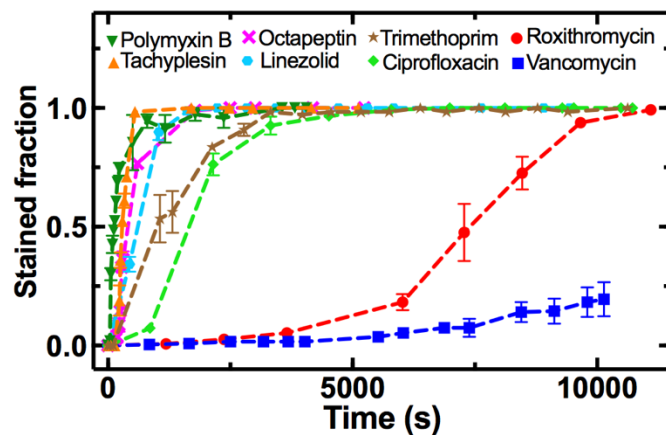


Figure S5. Temporal dependence of the fraction of *E. coli* stained by fluorescent derivatives of polymyxin B (downwards triangles), tachyplesin (upwards triangles), octapeptin (crosses), linezolid (hexagons), trimethoprim (stars), ciprofloxacin (diamonds), roxithromycin (circles) or vancomycin (squares). The stained fraction at each time point is defined as the ratio of the number of bacteria displaying a fluorescence distinguishable from the background over the total number of bacteria at that time point. Symbols and error bars are the mean and standard error of the mean values calculated by averaging the $N = 103, 128, 104, 115, 175, 122, 265, 236$ individual bacteria, respectively, from biological triplicate presented in Fig. S1.

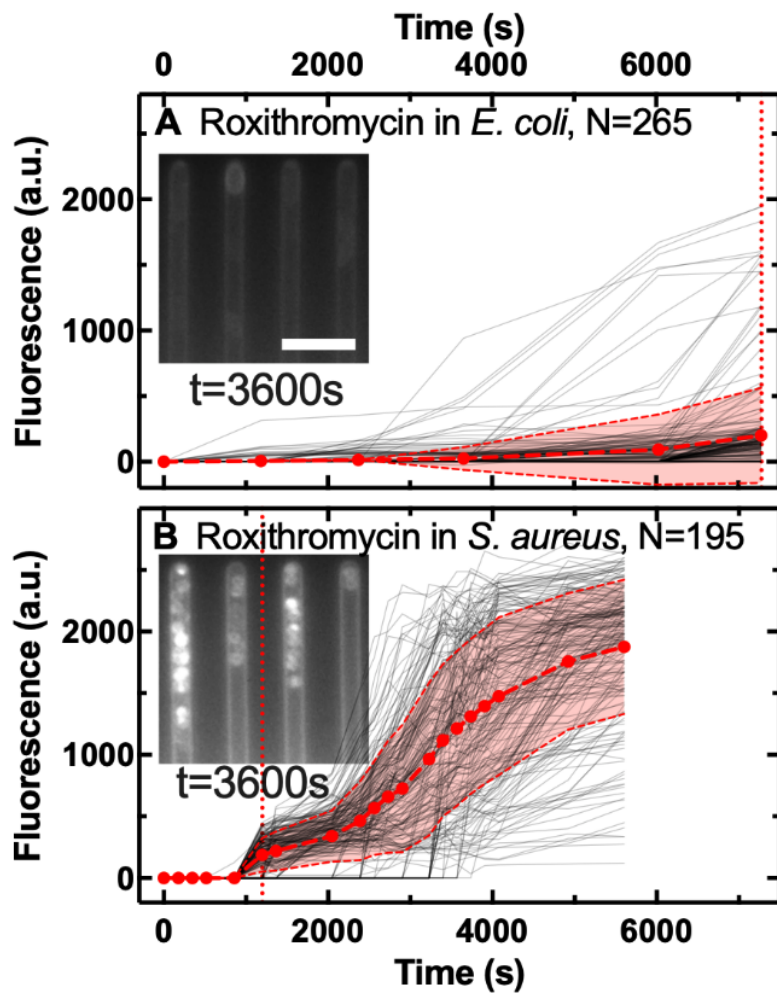


Figure S6. Accumulation of the fluorescent derivative of roxithromycin in **A)** $N = 265$ individual *E. coli* and **B)** $N = 195$ individual *S. aureus* (continuous lines), after adding the probe at $46 \mu\text{g mL}^{-1}$ extracellular concentration in M9 minimal medium from $t = 0$ onwards. Data were collated from biological triplicate. Fluorescence values were background subtracted and normalised by cell size. The symbols and shaded areas are the mean and standard deviation of the corresponding single-cell values. Insets: representative fluorescence images showing the accumulation of the fluorescent derivative of roxithromycin 3,600 s post addition to the bacteria hosting channels. Scale bar: 5 μm . The vertical dotted lines represent the time points at which the median of each dataset became larger than zero.

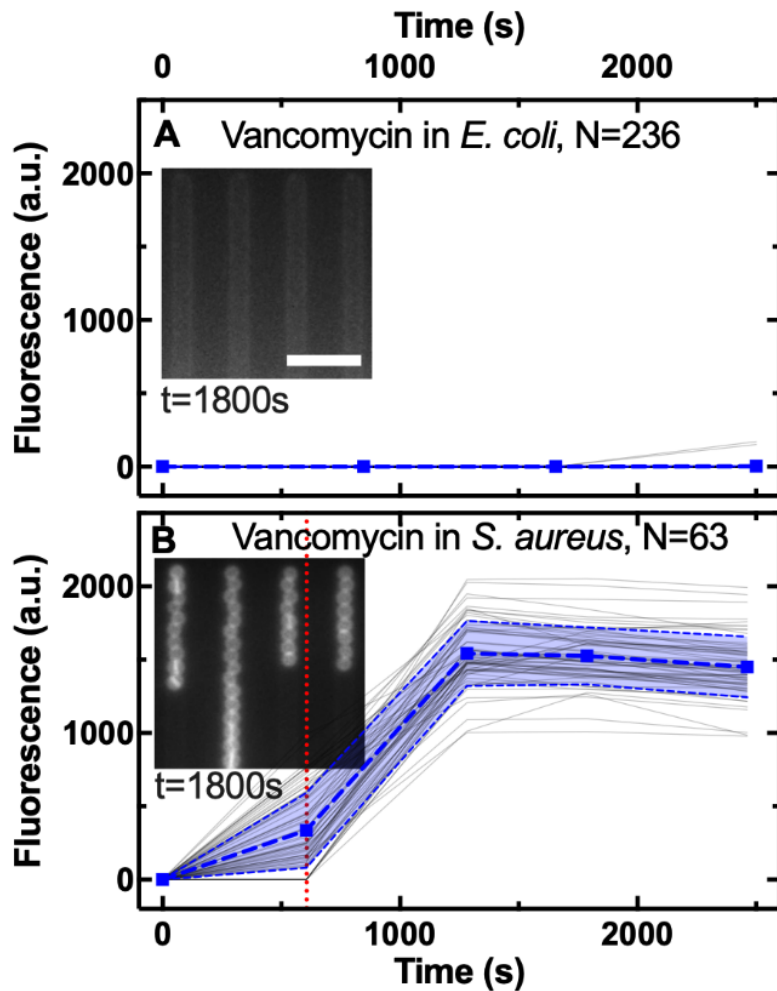


Figure S7. Accumulation of the fluorescent derivative of vancomycin in **A**) N = 236 individual *E. coli* and **B**) N = 63 individual *S. aureus* (continuous lines) cells, after adding the probe at 46 $\mu\text{g mL}^{-1}$ extracellular concentration in M9 minimal medium from $t = 0$ onwards. Data were collated from biological triplicate. Fluorescence values were background subtracted and normalised by cell size. The symbols and shaded areas are the mean and standard deviation of the corresponding single-cell values. Insets: representative fluorescence images showing the accumulation of the fluorescent derivative of roxithromycin 1,800 s post addition to the bacteria hosting channels. Scale bar: 5 μm . The vertical dotted lines represent the time points at which the median of each dataset became larger than zero.

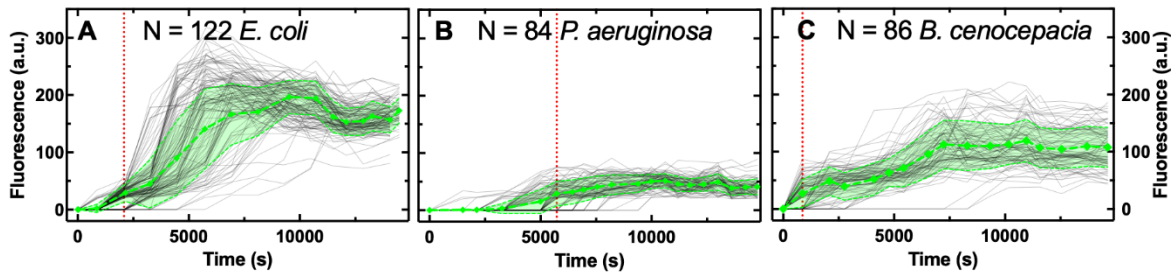


Figure S8. Accumulation of the fluorescent derivative of ciprofloxacin in **A**) $N = 122$ individual *E. coli*, **B**) $N = 84$ individual *P. aeruginosa* and **C**) $N = 86$ individual *B. cenocepacia* (continuous lines) cells, after adding the probe at $46 \mu\text{g mL}^{-1}$ extracellular concentration in M9 minimal medium from $t = 0$ onwards. Data were collated from biological triplicate. Fluorescence values were background subtracted and normalised by cell size. The symbols and shaded areas are the mean and standard deviation of the corresponding single-cell values. The vertical dotted lines represent the time points at which the median of each dataset became larger than zero. As expected ciprofloxacin-NBD accumulated to a significantly lower extent in *P. aeruginosa* since it lacks general porins, thus displaying a lower permeability compared to *E. coli* and *B. cenocepacia*(1).

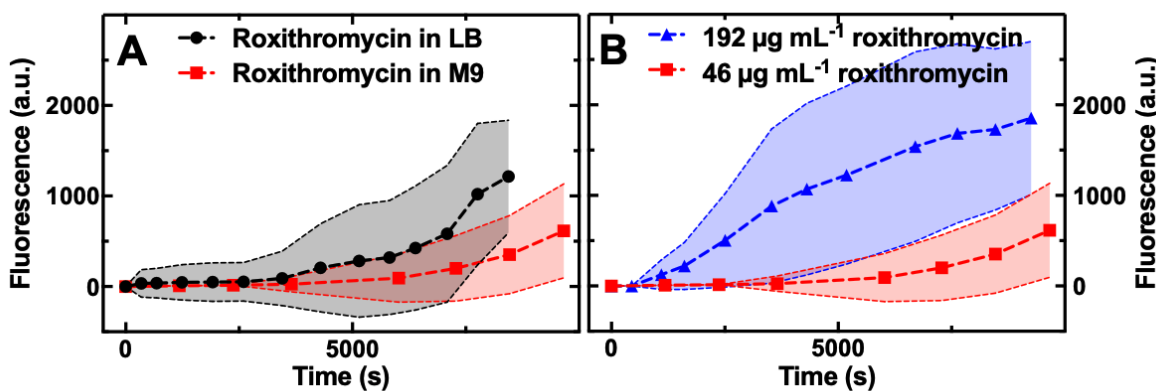


Figure S9. **A)** Accumulation of the fluorescent derivative of roxithromycin in LB (circles) or M9 medium (squares) drug milieu delivered to $N = 46$ and 265 individual *E. coli*, respectively, at an extracellular concentration of $46 \mu\text{g mL}^{-1}$. **B)** Accumulation of the fluorescent derivative of roxithromycin delivered at a concentration of 192 (triangles) and 46 (squares) $\mu\text{g mL}^{-1}$ in a M9 medium drug milieu to $N = 110$ and 265 individual *E. coli*, respectively. In both figures data were collated from biological triplicate and fluorescence values were background subtracted and normalised by cell size. The symbols and shaded areas represent the mean and standard deviation of the corresponding single-cell values.

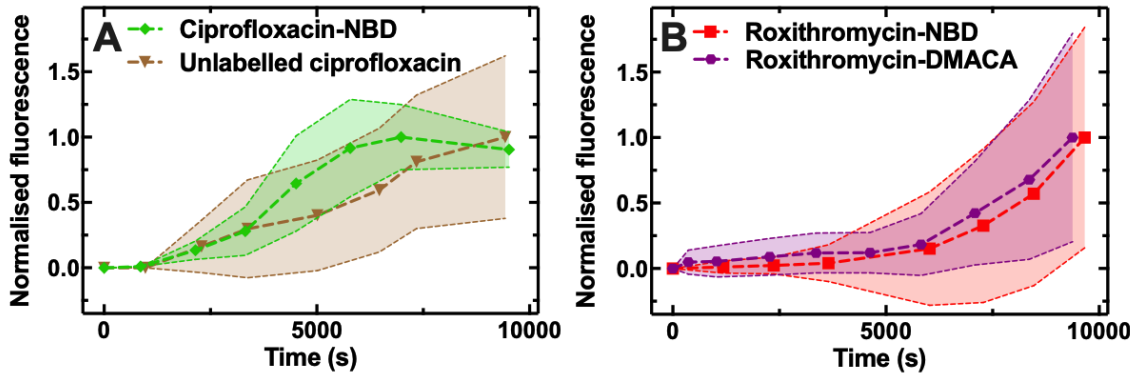


Figure S10. **A)** Accumulation of unlabelled ciprofloxacin (triangles) and of the fluorescent derivative ciprofloxacin-NBD (diamonds) delivered to $N = 48$ and 122 individual *E. coli*, respectively, at an extracellular concentration of 200 and 46 $\mu\text{g mL}^{-1}$ in M9 medium, respectively. It is worth noting that unlabelled ciprofloxacin was not detectable neither extracellularly nor intracellularly at concentrations below 200 $\mu\text{g mL}^{-1}$. **B)** Accumulation of the fluorescent derivatives roxithromycin-NBD (squares) and roxithromycin-DMACA (hexagons) at an extracellular concentration of 46 $\mu\text{g mL}^{-1}$ in a M9 medium drug milieu delivered to $N = 265$ and 77 individual *E. coli*, respectively. In both figures data were collated from biological triplicate and fluorescence values were background subtracted and normalised by cell size. The symbols and shaded areas are the mean and standard deviation of the corresponding single-cell values normalised to the maximum mean fluorescence value in each dataset.

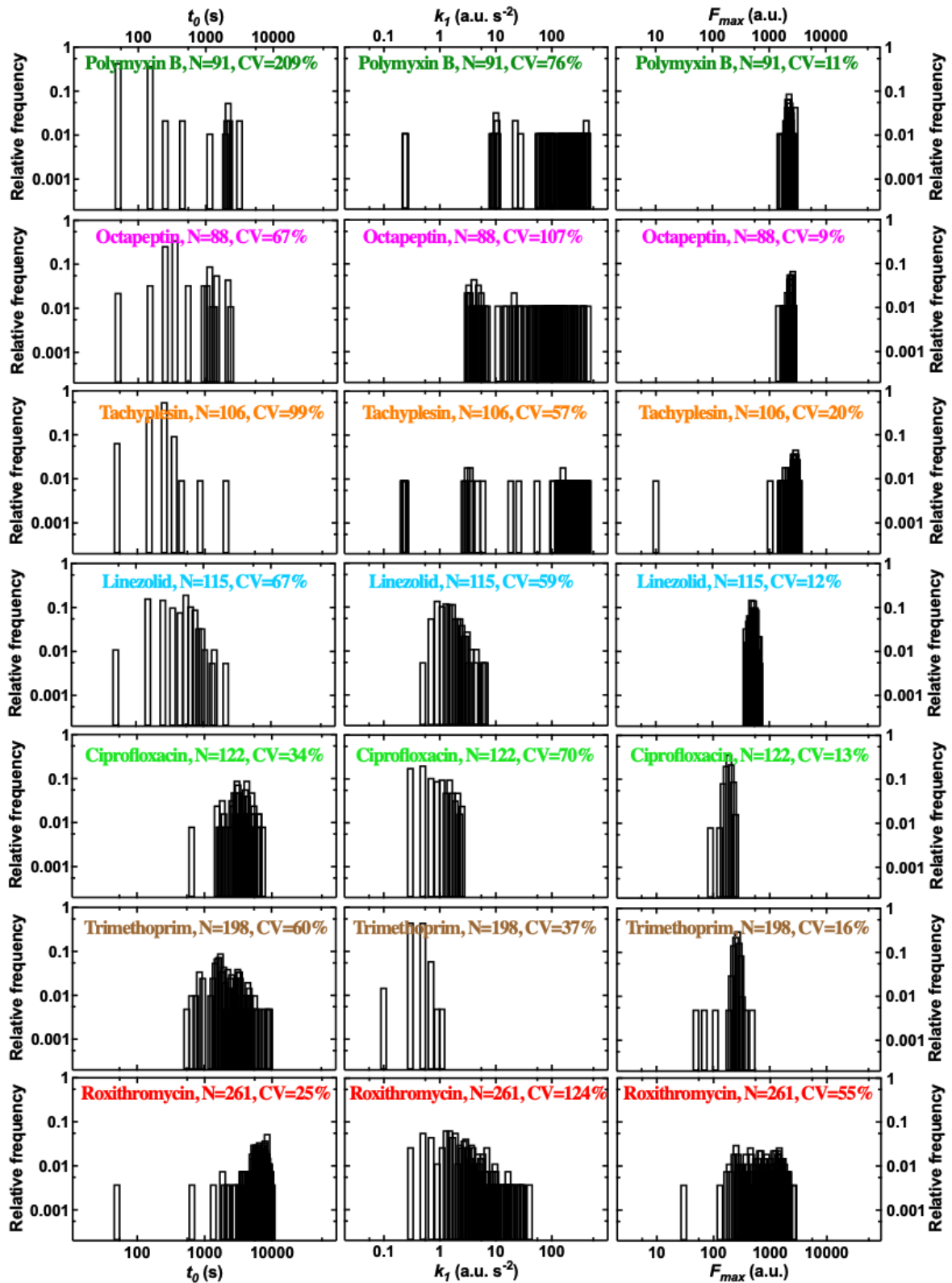


Figure S11. Distributions of t_0 , k_1 and F_{max} kinetic parameters describing the accumulation of the fluorescent derivatives of polymyxin B, octapeptin, tachyplesin, linezolid, ciprofloxacin, trimethoprim and roxithromycin (from top to bottom, respectively). These parameters were inferred by fitting the single-cell data reported in Fig. S1 using our mathematical model (see Methods). Data for which the fitting algorithm returned divergent transitions were not reported and typically represented less than 1% of the data (compare N here and in Fig. S1). t_0 is the inferred accumulation onset, i.e. the time at which each bacterium fluorescence became distinguishable from background fluorescence, k_1 is the inferred rate of uptake, F_{max} is the inferred fluorescence saturation level at steady-state. CV is the coefficient of variation of the single-cell values in each dataset.

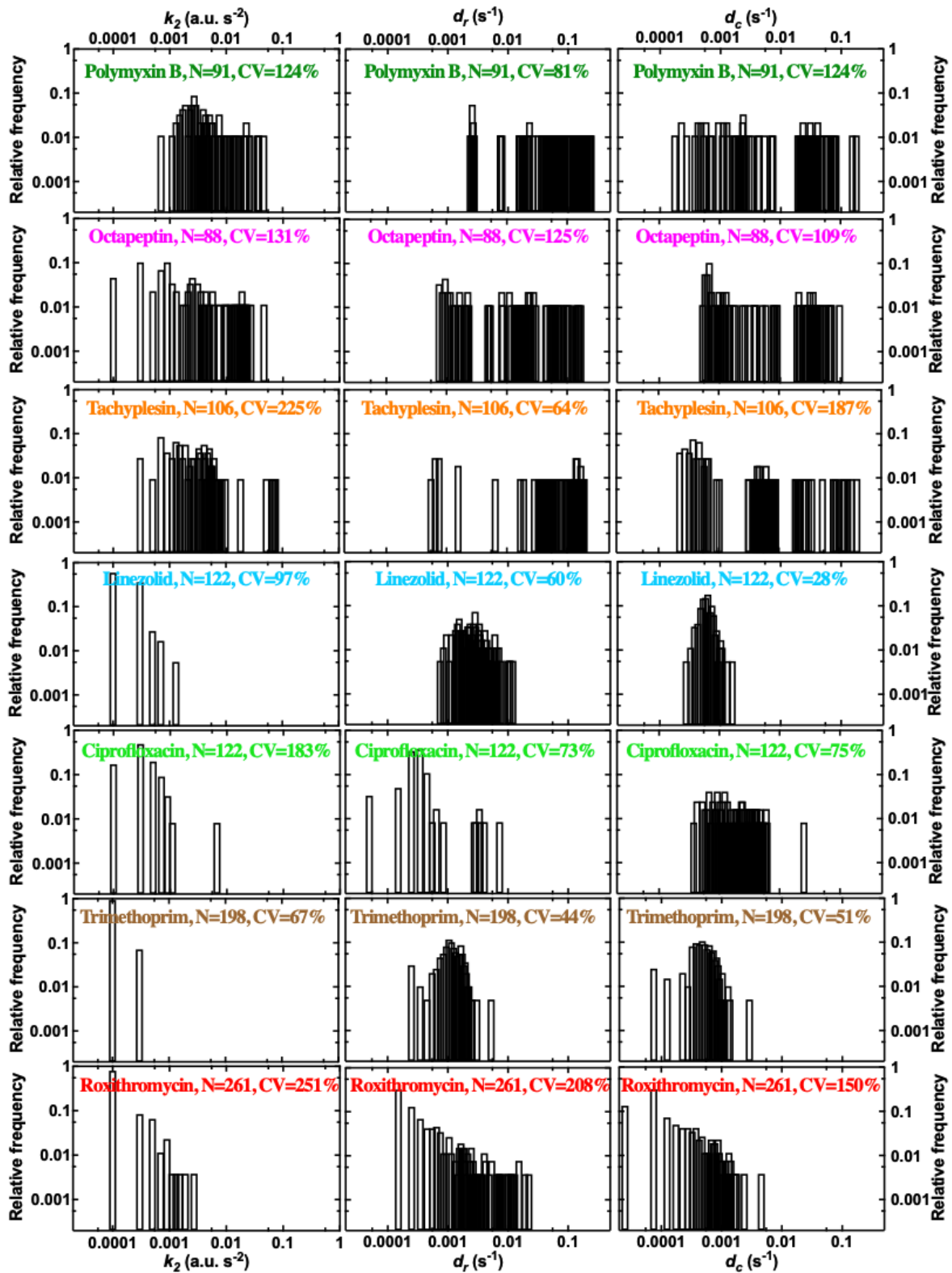


Figure S12. Distributions of k_2 , d_r and d_c kinetic parameters describing the accumulation of fluorescent antibiotic derivatives of polymyxin B, octapeptin, tachyplesin, linezolid, ciprofloxacin, trimethoprim and roxithromycin (from top to bottom, respectively). These parameters were inferred by fitting the single-cell data reported in Fig. S1 using our mathematical model (see Methods). Data for which the fitting algorithm returned divergent transitions were not reported and typically represented less than 1% of the data (compare N here and in Fig. S1). k_2 is the inferred adaptive inhibitory rate constant that describes the dip we observed in some single-cell trajectories in Fig. S1, d_r is the drug loss rate constant, d_c is the dampening rate constant. CV is the coefficient of variation of the single-cell values in each dataset. Membrane targeting antibiotic probes displayed, on average, a higher adaptive inhibitory rate constant ($k_2 = 0.006$, 0.007 and 0.006 a.u. s^{-2} for tachyplesin, polymyxin B and octapeptin, respectively) compared to antibiotics with intracellular targets ($k_2 = 0.0001$, 0.00005 , 0.0003 and 0.0001 s for linezolid, trimethoprim, ciprofloxacin and roxithromycin, respectively). Remarkably, we found notable cell-to-cell differences in k_2 across all investigated drugs with a maximum CV of 251% for roxithromycin and a minimum CV of 67% for trimethoprim. Membrane targeting antibiotic probes also displayed, on average, a higher drug loss rate constant ($d_r = 0.09$, 0.09 and 0.03 s^{-1} for tachyplesin, polymyxin B and octapeptin, respectively) compared to antibiotics with intracellular targets ($d_r = 0.0003$, 0.001 , 0.0005 and 0.001 s for linezolid, trimethoprim, ciprofloxacin and roxithromycin, respectively). Remarkably, we found notable cell-to-cell differences in d_r across all investigated drugs with a maximum CV of 208% for roxithromycin and a minimum CV of 44% for trimethoprim. Membrane targeting antibiotic probes also displayed, on average, a higher dampening rate constant ($d_c = 0.009$, 0.01 and 0.009 s^{-1} for tachyplesin, polymyxin B and octapeptin, respectively) compared to antibiotics with intracellular targets ($d_c = 0.0006$, 0.0005 , 0.002 and 0.0003 s for linezolid, trimethoprim, ciprofloxacin and roxithromycin, respectively). Remarkably, we found notable cell-to-cell differences in d_c across all investigated drugs with a maximum CV of 187% for tachyplesin and a minimum CV of 28% for linezolid.

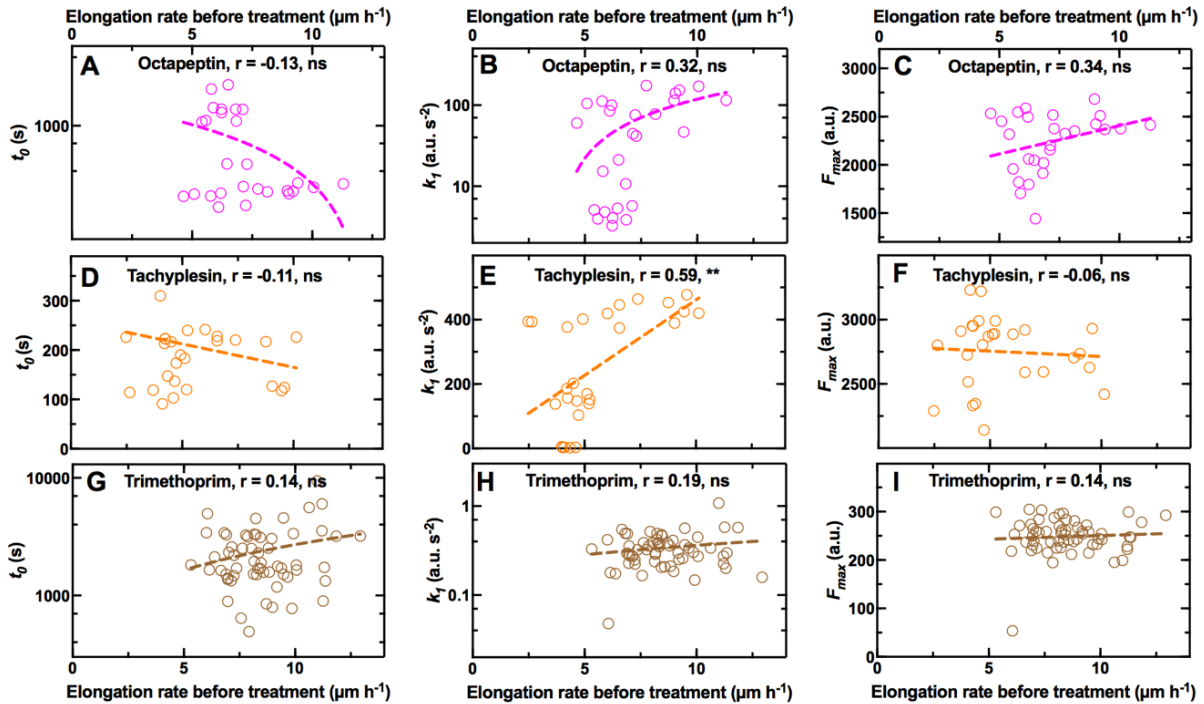


Figure S13. Interdependence between single-cell elongation rate before treatment and the onset t_0 , the rate k_1 , and the saturation F_{\max} in the accumulation of fluorescent derivatives of **A-C)** octapeptin, **D-F)** tachyplesin and **G-I)** trimethoprim, respectively. r is the Pearson correlation coefficient, **: p -value < 0.01 , ns: not significant, p -value > 0.05 . $N = 28$, 27 and 61 individual *E. coli* investigated for the accumulation of the fluorescent derivatives of octapeptin, tachyplesin, and trimethoprim, respectively, and collated from biological triplicate. In each experiment *E. coli* were grown for 2 h in the microfluidic device with continuous supply of fresh LB. During this 2 h growth period the elongation rate of each bacterium was measured between consecutive time points and the average elongation rate for each bacterium was calculated. At the end of this 2 h growth period one of the three fluorescent antibiotic derivatives above was continuously delivered for a 4 h treatment period in the microfluidic device at a concentration of $46 \mu\text{g mL}^{-1}$ in M9 minimal medium. During this 4 h treatment period single-cell fluorescence data were obtained and dynamic accumulation parameters t_0 , k_1 and F_{\max} were inferred by fitting these single-cell data to our mathematical model (see Methods).

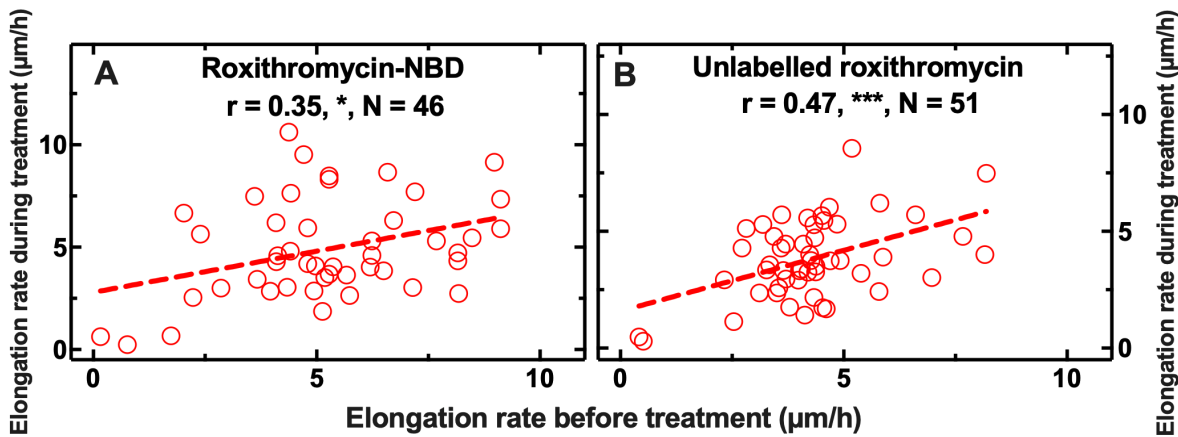
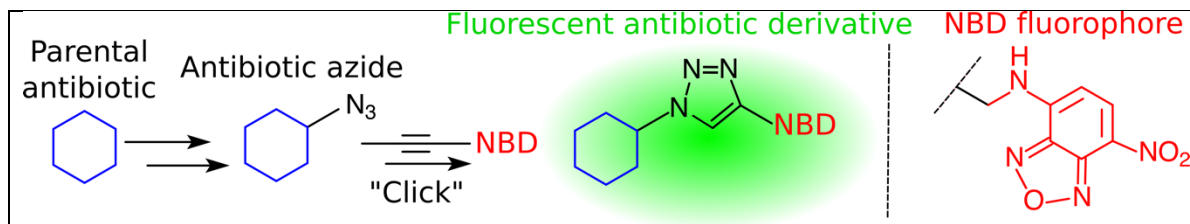


Figure S14. Interdependence between single-cell elongation rate before treatment and single-cell elongation rate during exposure to **A**) roxithromycin-NBD and **B**) unlabelled roxithromycin. r is the Pearson correlation coefficient, *: p-value < 0.05, **: p-value < 0.001. N = 46 and 51 individual *E. coli* investigated and collated from biological triplicate. In each experiment *E. coli* were grown for 2 h in the microfluidic device with continuous supply of fresh LB. During this 2 h growth period the elongation rate of each bacterium was measured between consecutive time points and the average elongation rate for each bacterium was calculated. At the end of this 2 h growth period, 46 $\mu\text{g mL}^{-1}$ roxithromycin-NBD or unlabelled roxithromycin dissolved in LB was continuously delivered for a 4 h treatment period in the microfluidic device. During this 4 h treatment period the elongation rate of each bacterium was measured as indicated above.



Antibiotic probe	Compartment	MW (g/mol)	logP	MIC ($\mu\text{g/mL}$)	Fold change
Polymyxin B-NBD	Membrane	1449	-2.5	1	1
Octapeptin-NBD	Membrane	1304	-0.4	4	1
Tachyplesin-NBD	Membrane	2523	-2.7	1	1
Vancomycin-NBD	Cell wall	1650	-2.6	>192	1
Linezolid-NBD	Cytoplasm	638	0.7	134	1.4
Roxithromycin-NBD	Cytoplasm	1064	3.1	192	3
Ciprofloxacin-NBD	Cytoplasm	633	-1.1	8	256
Trimethoprim-NBD	Cytoplasm	577	0.9	64	64

Table S1. List of fluorescent antibiotic derivatives (obtained by linking the parental antibiotic to nitrobenzoxadiazole, NBD, see Methods), the bacterial compartment where their target is located, their molecular weight (MW) after linkage to NBD, their partition coefficient (logP), their measured minimum inhibitory concentration (MIC) against *E. coli* BW25113, and the fold-change compared to the MIC measured for each corresponding parental antibiotic (see Methods). MIC data were collated from biological triplicate.

Antibiotics	Pearson correlation coefficients and significance		
	<i>t</i> ₀ vs <i>k</i> ₁	<i>t</i> ₀ vs <i>F</i> _{max}	<i>k</i> ₁ vs <i>F</i> _{max}
Polymyxin B	-0,51, ***	-0,54, ***	0,56, ***
Octapeptin	-0,46, ***	-0,61, ***	0,20, ns
Tachyplesin	-0,13, ns	-0,10, ns	-0,01, ns
Linezolid	0,03, ns	-0,21, **	0,05, ns
Ciprofloxacin	-0,12, ns	-0,11, ns	0,29, ***
Trimethoprim	0,06, ns	-0,32, ***	0,11, ns
Roxithromycin	-0,22, ***	-0,10, ns	0,41, ***
All antibiotics	-0,40, ***	-0,27, ***	0,65, ***

Table S2. Pearson correlation coefficients and significance of the correlation between *t*₀ and *k*₁, *t*₀ and *F*_{max} and *k*₁ and *F*_{max} for the accumulation in single *E. coli* of all the fluorescent antibiotic derivatives investigated

(apart from vancomycin) in individual *E. coli*. Data from Fig. S11 were used for these statistical comparisons.

****: p-value < 0.0001, ***: p- value < 0.001, **: p-value < 0.01, *: p-value < 0.05, ns: not significant, p-value > 0.05.

Membrane genes	Transcript reads						
<i>ompA</i>	60955	<i>mltA</i>	398	<i>acrZ</i>	47	<i>yaiO</i>	6
<i>ompC</i>	57458	<i>yncD</i>	388	<i>yfIB</i>	39	<i>cusB</i>	6
<i>ompX</i>	19210	<i>lolB</i>	345	<i>cusA</i>	39	<i>yehB</i>	5
<i>lptD</i>	10977	<i>nlpD</i>	326	<i>macB</i>	36	<i>bgfH</i>	5
<i>tolC</i>	4722	<i>mdtK</i>	312	<i>yhcD</i>	33	<i>wza</i>	5
<i>flhA</i>	4360	<i>yiaD</i>	292	<i>fimD</i>	31	<i>blc</i>	5
<i>bamA</i>	4237	<i>nplE</i>	291	<i>acrF</i>	30	<i>acrE</i>	5
<i>acrB</i>	4044	<i>sepA</i>	289	<i>pgaA</i>	29	<i>yfgH</i>	4
<i>bamB</i>	3796	<i>yraP</i>	256	<i>mdtL</i>	28	<i>nanC</i>	4
<i>ompF</i>	3650	<i>emtA</i>	252	<i>mdtG</i>	28	<i>yqhH</i>	4
<i>slyB</i>	3516	<i>ydiY</i>	241	<i>mdtF</i>	27	<i>phoE</i>	4
<i>nlpI</i>	3367	<i>tamA</i>	236	<i>yfaL</i>	25	<i>mdtQ</i>	3
<i>fadL</i>	2612	<i>yjgL</i>	222	<i>gfcD</i>	24	<i>yliI</i>	3
<i>ompT</i>	2601	<i>mdfA</i>	220	<i>gspD</i>	23	<i>ompN</i>	3
<i>mipA</i>	2289	<i>ynfB</i>	220	<i>yraJ</i>	22	<i>mdtO</i>	3
<i>mltD</i>	2045	<i>ypjA</i>	220	<i>gfcE</i>	22	<i>cusC</i>	2
<i>fecA</i>	2009	<i>pgpB</i>	193	<i>flgG</i>	22	<i>cusF</i>	2
<i>tsx</i>	1971	<i>mltC</i>	187	<i>mdtJ</i>	21	<i>mdtP</i>	2
<i>pal</i>	1945	<i>mdtC</i>	166	<i>mdtD</i>	19	<i>yfeN</i>	2
<i>skp</i>	1553	<i>lpoB</i>	155	<i>ydeT</i>	17	<i>mdtN</i>	2
<i>bamD</i>	1544	<i>macA</i>	153	<i>slp</i>	16	<i>csgF</i>	2
<i>acrA</i>	1505	<i>loiP</i>	137	<i>yceK</i>	16	<i>yjbF</i>	1
<i>mepS</i>	1303	<i>mltF</i>	134	<i>mdtI</i>	13	<i>csgB</i>	1
<i>lpp</i>	1168	<i>yaiW</i>	131	<i>chiP</i>	12	<i>envY</i>	1
<i>borD</i>	1167	<i>bhsA</i>	119	<i>pagP</i>	11	<i>ybgQ</i>	1
<i>nmpC</i>	1146	<i>pqiC</i>	114	<i>yedS</i>	11	<i>acrS</i>	1
<i>cirA</i>	1127	<i>rsxG</i>	107	<i>yjbH</i>	10	<i>uidC</i>	1
<i>bamC</i>	1123	<i>rcsF</i>	105	<i>rhsD</i>	9	<i>csgE</i>	0
<i>ygiB</i>	1115	<i>yfaZ</i>	101	<i>elfC</i>	9	<i>ompL</i>	0
<i>flu</i>	1064	<i>cusR</i>	99	<i>rhsB</i>	9	<i>ompG</i>	0
<i>lptA</i>	1052	<i>nfrA</i>	98	<i>yfcU</i>	8	<i>rzoD</i>	0
<i>mlaA</i>	1042	<i>cusS</i>	92	<i>lamB</i>	8	<i>rzoR</i>	0
<i>ybhC</i>	1021	<i>acrR</i>	85	<i>pgaB</i>	8	<i>yddL</i>	0
<i>lptE</i>	924	<i>yghG</i>	83	<i>sfnD</i>	8	<i>appX</i>	ND
<i>bamE</i>	732	<i>flhE</i>	81	<i>htrE</i>	8	<i>bcsC</i>	ND
<i>rlpA</i>	637	<i>amiD</i>	80	<i>mdtH</i>	7	<i>epcC</i>	ND
<i>lpoA</i>	620	<i>yddB</i>	76	<i>yiaT</i>	7	<i>qseG</i>	ND
<i>flu</i>	607	<i>acrD</i>	72	<i>mliC</i>	7	<i>ychO</i>	ND
<i>btuB</i>	489	<i>ecnB</i>	69	<i>mdtE</i>	7	<i>ypjB</i>	ND
<i>tamB</i>	408	<i>mdtB</i>	64	<i>flgH</i>	7	<i>yzcX</i>	ND
<i>mltB</i>	406	<i>mdtA</i>	54	<i>csgG</i>	6		
<i>pldA</i>	404	<i>ecnA</i>	51	<i>hofQ</i>	6		
<i>ppk</i>	404	<i>mdtM</i>	49	<i>ompW</i>	6		

Table S3. List of genes encoding outer membrane proteins (i.e. porins) and efflux pumps compiled using EcoCyc as previously reported(2), alongside their transcript reads after a 2 h growth period in LB (i.e. the time point at which antibiotic treatment starts in our microfluidic experiments) measured via RNA-sequencing as previously reported(3). Note that it has been reported that permeability of solutes through

OmpA (with the most highly expressed transcripts) is a hundred fold lower compared to that through OmpC(4) (with the second most highly expressed transcripts), hence we decided to investigate the role played by OmpC in the heterogeneity in the intracellular accumulation of roxithromycin (Fig. 5E).

References

1. V. V. Rybenkov, *et al.*, The Whole Is Bigger than the Sum of Its Parts: Drug Transport in the Context of Two Membranes with Active Efflux. *Chem. Rev.* **121**, 5597 (2021).
2. K. E. Kortright, B. K. Chan, P. E. Turner, High-throughput discovery of phage receptors using transposon insertion sequencing of bacteria. *Proc. Natl. Acad. Sci. U. S. A.* **117**, 18670–18679 (2020).
3. A. Smith, *et al.*, The culture environment influences both gene regulation and phenotypic heterogeneity in *Escherichia coli*. *Front. Microbiol.* **9**, 1739 (2018).
4. E. Sugawara, H. Nikaido, Pore-forming activity of OmpA protein of *Escherichia coli*. *J. Biol. Chem.* **267**, 2507–2511 (1992).

Movie S1.

Real-time accumulation of the fluorescent derivative of roxithromycin in individual *Escherichia coli* and *Staphylococcus aureus* bacteria (top and bottom panels, respectively).

Movie S2.

Real-time accumulation of the fluorescent derivatives of vancomycin and roxithromycin in individual *Staphylococcus aureus* bacteria (top and bottom panels, respectively).